

## Size, shape, and composition of luminescent species in oxidized Si nanocrystals and H-passivated porous Si

S. Schuppler,\* S. L. Friedman,<sup>†</sup> M. A. Marcus, D. L. Adler,<sup>‡</sup> and Y.-H. Xie  
*AT&T Bell Laboratories, Murray Hill, New Jersey 07974*

F. M. Ross

*National Center for Electron Microscopy, Lawrence Berkeley Laboratory, Berkeley, California 94720*

Y. J. Chabal, T. D. Harris, L. E. Brus, W. L. Brown, E. E. Chaban, P. F. Szajowski, S. B. Christman, and P. H. Citrin<sup>§</sup>  
*AT&T Bell Laboratories, Murray Hill, New Jersey 07974*

(Received 13 March 1995)

Near-edge and extended x-ray-absorption fine-structure measurements from a wide variety of oxidized Si nanocrystals and H-passivated porous Si samples, combined with electron microscopy, ir absorption, forward recoil scattering, and luminescence emission data, provide a consistent structural picture of the species responsible for the luminescence observed in these systems. For porous Si samples whose luminescence wavelengths peak in the visible region, i.e., at  $< 700$  nm, their mass-weighted-average structures are determined here to be particles (not wires) whose short-range character is crystalline and whose dimensions—typically  $< 15$  Å—are significantly smaller than previously reported or proposed. Results are also presented which demonstrate that the observed visible luminescence is not related to either a photo-oxidized Si species in porous Si or an interfacial suboxide species in the Si nanocrystals. The structural and compositional findings reported here depend only on sample luminescence behavior, not on how the luminescent particles are produced, and thus have general implications in assigning quantum confinement as the mechanism responsible for the visible luminescence observed in both nanocrystalline and porous silicon.

### I. INTRODUCTION

Silicon lies at the heart of almost all microelectronics, but its indirect band gap and correspondingly poor luminescence properties make it ineffective for light-emitting devices.<sup>1,2</sup> Optoelectronic hybrid designs involving the integration of Si with III-V compounds are costly and difficult to fabricate, providing strong incentive to look for more efficient light-emitting forms of Si.<sup>3</sup> A variety of approaches for achieving this include alloying with Ge,<sup>4,5</sup> doping with rare-earth metals like Er,<sup>6,7</sup> and anodic etching with HF.<sup>8,9</sup>

Anodic etching is a particularly simple and therefore attractive procedure that can lead to Si porosities as large as 80–85%.<sup>10,11</sup> The so-produced porous Si (por-Si) is typically found to photoluminescence in the visible with quantum efficiencies of several percent at room temperature.<sup>12</sup> Typical transmission-electron-microscopy (TEM) measurements from such por-Si samples reveal structures with dimensions of 20–50 Å.<sup>13–16</sup> These initial observations, and the pioneering proposal<sup>8,9</sup> that quantum size effects control the optical properties of por-Si, have stimulated an enormous amount of research in this area over the last several years.<sup>17</sup> Theoretical and experimental efforts in related fields,<sup>18–20</sup> e.g., Si nanoclusters and polymers, have also increased and taken on added importance since the initial investigations.<sup>8–16</sup> Apart from technological motivations, these related studies address more general issues dealing with fundamental properties of nanosized Si.

Given this large and varied body of work on por-Si, there still remains a basic lack of knowledge regarding the structure and composition of the species actually responsible for the optical activity. At least five factors contribute to this uncertainty: (1) Heterogeneity: Anodic etching in HF produces material consisting of macroscopic regions of unetched *c*-Si separating areas of variously sized nanoscale por-Si structures.<sup>13–16,21–27</sup> The observed luminescence wavelength and efficiency depend on the size distribution of these nanostructures, and the distribution varies with details of the etching conditions and of the starting Si-wafer properties. (2) Chemical reactivity: The nanostructure surfaces in freshly prepared por-Si are passivated with H, and these are generally unstable with respect to subsequent exposure to air or photoexciting radiation.<sup>8,28–31</sup> The presence—or absence—of H or O on the surfaces of nanosized Si structures could in principle affect the luminescence properties of the por-Si samples. (3) Penetration depth: The photoexciting radiation producing the maximum luminescence intensity in por-Si lies in the range of 350–400 nm,<sup>24</sup> which probes even 80% porosity samples no more than  $\sim 5000$  Å.<sup>32</sup> Therefore, within the total portion of etched Si, typically  $\leq 5$   $\mu\text{m}$ , the observed photoluminescence originates from a relatively small near-surface region, and this overall configuration is not well suited for standard microscopy or diffraction techniques from as-prepared material. (4) Characteristic sizes: Optically active structures  $< 20$  Å are beyond practical detection limits of standard microscopy and diffraction

methods. Accordingly, the smallest dimensions for structures observed and reported with these techniques are  $\geq 20$  Å. (5) Computational uncertainties: Various theoretical studies correlating band gap with Si size report nanoscale particle or wire dimensions for a given band gap which vary by more than 100%.<sup>33–46</sup> Little attention is usually given to the size regime of structures  $< 20$  Å.

In the present work, which expands upon an earlier Letter,<sup>47</sup> we apply Si *K*-edge absorption spectroscopy to a series of oxidized Si nanocrystals and to a variety of anodically grown por-Si samples. This approach minimizes or avoids the inherent experimental difficulties associated with identifying and characterizing the optically active species in these systems. In particular, the x-ray-absorption measurements probe optically relevant sample depths (i.e., within 2500 Å from the surface<sup>48</sup>), they identify the existence and amount of any O-containing Si species to within  $\sim 1\%$ ,<sup>49</sup> and they structurally characterize Si moieties with dimensions  $\lesssim 5$  Å.<sup>50</sup> Using the known sizes and shapes of the Si nanocrystals, combined with luminescence, TEM, ir-absorption, and forward recoil scattering (FRS) measurements from a series of por-Si samples, the x-ray-absorption results establish average sizes for the visible-luminescing species in por-Si that are substantially smaller than those reported previously.<sup>13–16,21–27</sup> A combination of x-ray- and/or ir-absorption and luminescence data from por-Si and nanocrystalline Si samples also show that in both systems the observed visible luminescence is unrelated to any O-containing Si species.<sup>51–60</sup> Furthermore, the importance of extended wirelike shapes<sup>8,9</sup> for visible-light-emitting Si structures in por-Si is ruled out in favor of particles.<sup>11,61</sup> Reasons for apparent discrepancies between the structures, compositions, and luminescent properties reported in other studies and those determined in this work are discussed. Finally, the inferred band-gap versus size correlation found here supports the original proposal<sup>8,9</sup> that quantum size effects are responsible for the efficient room-temperature luminescence. The actual sizes of the visibly emitting species determined from this work are, however, significantly smaller than those calculated by most groups,<sup>34–38,41–46</sup> but are in good agreement with results of recent theoretical work.<sup>62,63</sup>

## II. EXPERIMENT

### A. Sample preparation

The oxidized Si nanocrystals, ox-Si<sub>x</sub>, were made by homogeneous nucleation in a high-pressure flow of He from pyrolysis of disilane at 700–1000°C with subsequent oxidation in O<sub>2</sub> at 700–1000°C for about 30 ms.<sup>64</sup> The resulting aerosol was bubbled through ethylene glycol to create nanocrystalline colloids. Four narrowed fractions of nanocrystallites, labeled in this work *l* (large), *m* (medium), *s* (small), and *vs* (very small), were obtained using size-selective precipitation. All of these O-passivated structures are insensitive to air exposure.

Preparation of the four different types of por-Si samples studied here, referred to as *A*, *B*, *C*, and *D*, follow in spirit recipes reported in Refs. 16, 24, and 65. Essential

details of the various preparations are summarized in Table I. Samples of each type that were prepared and characterized several different times over a period of two years consistently gave reproducible results. Vacuum or inert-gas transports were used to minimize O contamination in the handling of samples. Air exposure of the freshly prepared H-passivated samples was limited to  $< 10$  min in all x-ray absorption and FRS measurements, and most of the luminescence and ir-absorption experiments.

### B. Transmission-electron-microscopy (TEM) measurements

The oxidized Si nanocrystals were characterized with TEM using a JEOL 2000-FX operated at 200 keV. Samples were collected by colloid evaporation onto holey carbon films. The por-Si layers were characterized for low magnification studies using a JEOL 200CX at 200 kV, and for lattice imaging using the 800-kV Berkeley Atomic Resolution Microscope with 1.6-Å resolution. Cross-sectional specimens with the foil normal along [110] were prepared using conventional methods, with final ion milling carried out at 77 K using 5-kV Ar<sup>+</sup> ions incident at 16°. Fragments of each film, which had been scraped off with a razor blade and dispersed onto a lacy carbon grid, were examined as well. (This method<sup>16</sup> avoids artifacts due to ion milling, but it is not usually possible to determine where in the film a given fragment originated.) For each film, both cross-sectional and plan-view images of several representative fragments were obtained.

### C. X-ray-absorption measurements

The Si *K*-edge absorption measurements were performed at the National Synchrotron Light Source using the AT&T Bell Laboratories X15B beamline<sup>66</sup> and a monochromator with InSb(111) crystals. The samples were kept at 77 K to minimize effects of thermal disorder.<sup>50</sup> All data from por-Si were obtained using total electron yield detection, whose effective sampling depth in bulk Si is  $< 500$  Å.<sup>48</sup> From this we estimate the sampling depth in 80%-porosity material to be  $< 2500$  Å, a value well matched to the depth from which visible luminescence is generated.<sup>32</sup> Oxygen contamination in the por-Si samples could be readily identified in the x-ray absorption spectra (see below) and was found to be negligible in the freshly prepared samples, handled as described above. The absence of detectable absorption from SiO<sub>2</sub> implies concentrations below 1%.<sup>49</sup>

The ox-Si<sub>x</sub> samples were prepared for x-ray-absorption measurements by transferring them as colloidal suspen-

TABLE I. Parameters for preparation of por-Si samples.

|          | <i>p</i> -Si(100)<br>(Ω cm) | HF in<br>ethanol<br>(%) | Current<br>density<br>(mA/cm <sup>2</sup> ) | Etching<br>time<br>(min) |
|----------|-----------------------------|-------------------------|---|--------------------------|
| <i>A</i> | $> 50$                      | 20                      | 20  | 60                       |
| <i>B</i> | $> 50$                      | 15                      | 25  | 12                       |
| <i>C</i> | $> 50$                      | 20                      | 20  | 5                        |
| <i>D</i> | $\sim 0.1$                  | 20                      | 10  | 30                       |

sions onto graphite substrates. The small amounts of Si in the *s* and *vs* samples required us to use Si *K* $\alpha$  fluorescence-yield rather than total-electron-yield detection as for the *m* and *l* samples. Care was taken to avoid self-absorption effects<sup>67</sup> in the fluorescence measurements.

#### D. Luminescence measurements

The luminescence emission and excitation spectra were obtained with a commercial fluorimeter equipped with double monochromators on both the excitation and emission branches. Spectral corrections for excitation intensities were achieved using a rhodamine B quantum converter, while for emission intensities a NIST-traceable standard spectral source was used to generate correction factors. Excitation radiation, with a typical power density of  $\sim 2$  mW/cm<sup>2</sup>, was at normal incidence to the samples. Detection of the emitted luminescence, using a photomultiplier sensitive to 920-nm radiation, was at slightly off-normal angles. All measurements were made on samples at room temperature. The ox-SiO<sub>x</sub> samples, in the form of colloidal suspensions in ethylene glycol, were sealed under air in suprasil tubes. With the exception of the photoinduced oxidation experiments (described in Sec. III B), all por-Si samples were measured in a cell under atmospheric pressure of Ar.

#### E. Forward recoil scattering measurements

The concentration of hydrogen in the por-Si samples was measured as a function of depth with FRS using 2.6-MeV He<sup>+</sup> ions at 15° grazing incidence on the sample surfaces.<sup>68</sup> Hydrogen atoms recoiling in the forward direction at 30° from the incident-beam direction (and thus also at 15° from the sample surface) were detected with a Si solid-state detector and energy analyzed to provide information about the depth from which they originated. An 11.8- $\mu$ m Mylar foil placed in front of the detector filtered out the dominant flux of forward-scattered He<sup>+</sup> ions while still transmitting the recoiling H atoms. Absolute concentrations of H in the por-Si samples were calibrated against recoil data from a reference bulk Si sample containing  $5 \times 10^{15}$  H atoms implanted at 30 keV.

#### F. Infrared-absorption measurements

The infrared-absorption measurements<sup>69</sup> were performed using two different configurations. The first is a traditional transmission geometry, where the normal-incident ir beam equally samples the entire volume of the por-Si layer and the underlying *c*-Si substrate. The second involves a Ge plate to confine the ir radiation through multiple internal reflections, making use of the evanescent nature of the radiation to probe only the por-Si region in contact with the Ge surface. As schematically illustrated in Fig. 1, one side of a Ge plate with 60°-beveled ends is pressed as close as possible (typical gap  $\sim 1000$  Å) against the por-Si surface. The ir radiation incident along the plate axis is refracted into the Ge, yielding an internal angle of incidence  $\theta_{\text{int}} = 67^\circ$ . The radia-

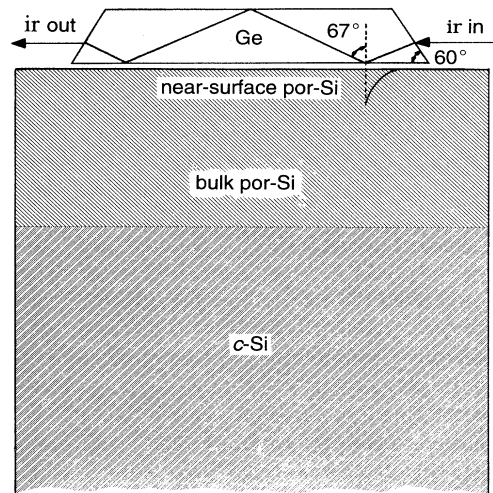


FIG. 1. Infrared absorption in the grazing-incidence configuration. Unlike conventional transmission geometry, in which incident ir radiation probes the entire sample, evanescent radiation from the internally reflected beam in a  $3.8 \times 1.5 \times 0.05$  cm<sup>3</sup> Ge plate preferentially probes the near-surface region of por-Si, typically  $< 0.5$   $\mu$ m.

tion is then totally internally reflected<sup>70</sup> multiple times before exiting the plate for detection. Most ir absorption occurs within a depth  $d/2$  from the surface, where  $d$  is the penetration depth of the evanescent field into the por-Si. This depth is given by<sup>70</sup>  $d = (\lambda/2\pi)[\sin^2\theta_{\text{int}} - (n_{\text{por-Si}}/n_{\text{Ge}})^2]^{-1/2}$ , where  $\lambda$  is the free-space ir radiation wavelength and  $n_{\text{Ge}}$  and  $n_{\text{por-Si}}$  are the effective ir refractive indices to Ge and por-Si. In our experiment,  $\lambda = 4.76$   $\mu$ m,  $n_{\text{Ge}} = 4.0$  and  $n_{\text{por-Si}} = 1.3$ ,<sup>71,72</sup> giving absorption confined within a  $< 0.5$ - $\mu$ m depth. This absorption profile is well studied for these por-Si experiments because it matches the near-surface region from which the luminescence originates.

### III. RESULTS

#### A. Nanocrystalline Si: TEM, NEXAFS, and luminescence data

The larger ox-Si<sub>x</sub> particles that emit in the 800–1000-nm range are easily seen by bright- and dark-field TEM imaging<sup>64</sup> as spherical-shaped structures with outer diameters of  $\sim 50$ – $100$  Å. An outer oxide shell of  $\sim 10$ -Å thickness surrounds the inner Si<sub>x</sub> cores of  $> 30$ -Å diameter. Lattice imaging and x-ray powder diffraction patterns<sup>64</sup> shows that the Si<sub>x</sub> cores are crystalline, with lattice constants unchanged from bulk *c*-Si (within experimental error). Accordingly, these nanosized Si<sub>x</sub> clusters are referred to as nanocrystals. Similar characterization of the smaller nanocrystals emitting in the 600–750-nm range is more difficult. TEM micrographs show them to be spherical as well, with outer diameters  $\lesssim 30$  Å. Their internal structure, however, is beyond the detection capabilities of either TEM or x-ray diffraction, so x-ray-absorption measurements are required.

In Fig. 2(a) we show Si *K* near-edge x-ray-absorption

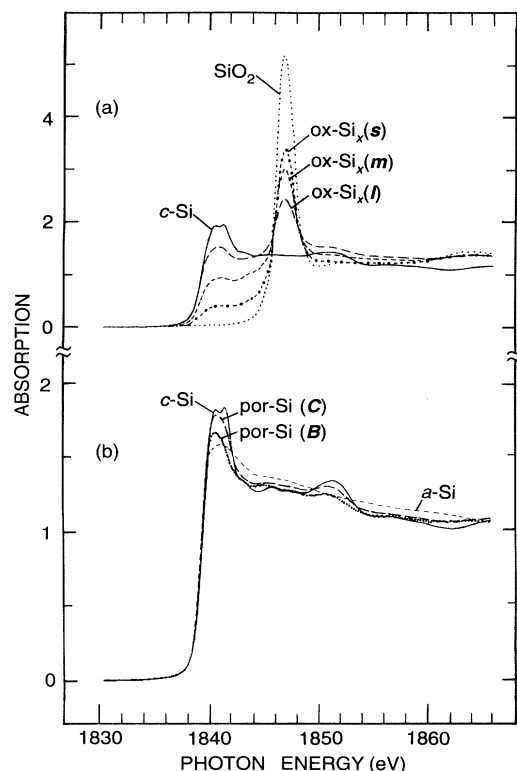


FIG. 2. (a) *K*-edge NEXAFS data from *c*-Si, SiO<sub>2</sub>, and oxidized Si nanocrystals of different sizes, labeled small (*s*), medium (*m*), and large (*l*). (b) NEXAFS data from *c*-Si, *a*-Si, and two differently prepared por-Si samples, labeled *B* and *C*. All data in (a) and (b) are normalized to unity edge jump.

fine-structure (NEXAFS) data from two of the larger oxidized Si nanocrystals characterized with TEM, labeled large (*l*) and medium (*m*), as well as a third sample labeled small (*s*). A fourth, very small (*vs*) sample was also measured, but omitted for clarity. Its spectrum is given in Fig. 3 and discussed below. Comparison in Fig. 2(a) with data from bulk SiO<sub>2</sub> and bulk *c*-Si (freshly HF-rinsed to remove the native oxide film) readily confirms that all three oxidized nanocrystalline samples contain both Si and SiO<sub>2</sub> components, as expected. In order to make meaningful comparisons between the relative amounts of each component in the different systems, the three ox-Si<sub>x</sub> and two model *c*-Si and SiO<sub>2</sub> spectra are normalized to a common "edge-jump" value, which is simply proportional to the atomic Si mass absorption coefficient.<sup>50</sup> (This value is measured > 100 eV above the Si *K* edge, where the x-ray absorption in each of the different systems is structureless, i.e., atomiclike.) After normalization, the smallest fraction of Si<sub>x</sub> relative to the total amount of Si absorption is seen to occur in the smallest of the three nanocrystallites, again as expected.

Apart from these qualitative observations, there are two other, more subtle features in the NEXAFS data. The first is that the two-peaked structure in the bulk *c*-Si data just above threshold, ~1840 eV, is not present in the ox-Si<sub>x</sub> spectra. This structure reflects the band structure of unfilled 3*p*-derived bands in the bulk crystalline

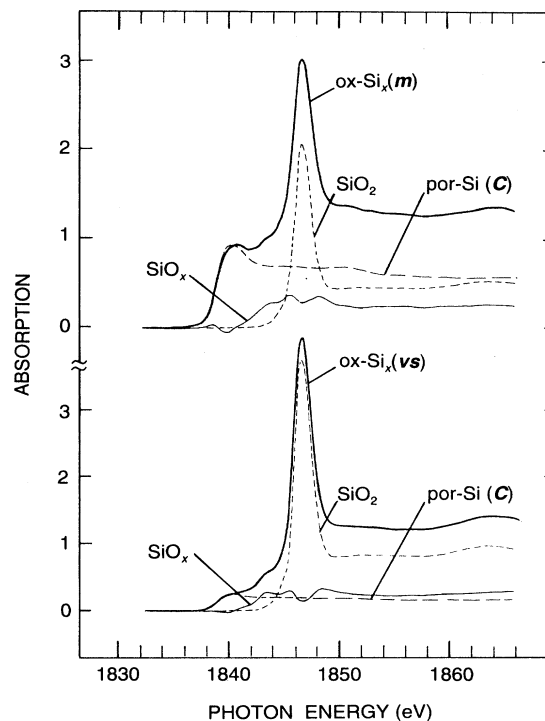


FIG. 3. Normalized Si *K*-edge NEXAFS data from two different sizes of oxidized Si nanocrystals, labeled medium (*m*) and very small (*vs*), shown to be comprised of three components: a SiO<sub>2</sub> outer shell, a Si inner core [modeled here by the por-Si (*C*) sample in Fig. 2(b)], and an interfacial suboxide species SiO<sub>x</sub>.

material,<sup>73</sup> and its absence in the nanocrystalline Si<sub>x</sub> reflects the fact that such bands are not yet fully formed,<sup>74</sup> even in the *l* crystallites. The second feature is the appearance of weak structure at  $\approx 1843$  eV between the *c*-Si and SiO<sub>2</sub> thresholds. It is somewhat more evident in the ox-Si<sub>x</sub>(*m*) data, and even more so in data from the very small (*vs*) nanocrystals. Both normalized spectra are displayed in Fig. 3.

The fact that the absorption edge of this weak structure lies between the edges of *c*-Si and SiO<sub>2</sub> and that there is only Si and O in this system together indicate that the structure corresponds to incompletely oxidized Si, i.e., SiO<sub>x</sub>. This species must be at the interface between the outer SiO<sub>2</sub> shell and the inner Si<sub>x</sub> core. We can obtain an approximate spectrum for the SiO<sub>x</sub> species by subtracting the contributions of the other two known components. [Rather than using the data from *c*-Si to model the Si<sub>x</sub> in these samples, we use the data from a por-Si sample in Fig. 2(b), described in Sec. III B, whose NEXAFS more closely resembles that of the nanocrystalline material.<sup>75</sup>] The result is shown as a thin solid line in Fig. 3. The overall edge shape and position<sup>76</sup> of the SiO<sub>x</sub> spectrum directly reflect its chemical composition, analogous to a chemical shift in core-level photoemission. That these spectral features are the same in the different nanocrystalline samples indicates there is *no* size-dependent change in interfacial stoichiometry.

The relative edge jumps of the Si<sub>x</sub>, SiO<sub>2</sub>, and SiO<sub>x</sub> con-

tributions are directly proportional to their relative mass fractions, and these can be converted into volume fractions using the corresponding densities.<sup>77</sup> From these volume fractions, from the outer diameters measured by TEM, and from the fact that the oxidized nanocrystals are spherical, we are then able to determine the mean inner diameters of the corresponding  $\text{Si}_x$  cores and the thicknesses of the intermediate  $\text{SiO}_x$  layer and the outer  $\text{SiO}_2$  layer. The results, including those from analysis of the ox- $\text{Si}_x(l)$  and ox- $\text{Si}_x(s)$  data, are given in Table II and are schematically illustrated in Fig. 4. We note that while the outer diameters of the oxidized nanocrystals have conservative error limits of  $\lesssim 20\%$  (reflecting the broad distribution of the size-separated particles<sup>64,78</sup>), the relative compositional mass fractions of Si determined by NEXAFS are much more precise. Thus, the percent error limits of the inner diameters and of the oxide-layer thicknesses are just the same as for the outer diameters (they have not been included in Table II for clarity; see below). Considering that in the four different ox- $\text{Si}_x$  samples the outer diameters vary by a factor of 4 and the inner diameters by a factor of 7, the thicknesses of both the intermediate  $\text{SiO}_x$  layer and the outer  $\text{SiO}_2$  layer remain remarkably constant. Furthermore, the  $\text{SiO}_x$ -layer thickness amounts to just about a monolayer, consistent with an abrupt interface.

The  $\text{Si}_x$  core diameters of the nanocrystals are plotted in Fig. 5 versus their peak luminescence energies measured at room temperature (typical luminescence spectra appear elsewhere<sup>64</sup>). The error bars that were omitted in Table II have been included in the figure. A well-defined trend is apparent: smaller  $\text{Si}_x$  particle sizes lead to higher emission energies. The constant thickness and stoichiometry of the interfacial suboxide layer, and the constant thickness of the outer  $\text{SiO}_2$  layer for very different  $\text{Si}_x$  diameters and peak luminescence energies, effectively rule out the suggestion<sup>59,60</sup> that  $\text{SiO}_x$  or  $\text{SiO}_2$  is the optically active species. This, coupled with the high ( $> 50\%$ ) quantum efficiencies of the nanocrystals at low temperatures<sup>64</sup> and the detailed characterization of their spectroscopic properties,<sup>78</sup> all clearly indicate that it is the inner  $\text{Si}_x$  cores which are responsible for the observed optical activity.

## B. Porous Si

### 1. TEM, NEXAFS, luminescence, and ir-absorption data

TEM images from samples *A*, *B*, and *C* appear to be qualitatively similar both at low and high magnification. The overall morphology of sample *B* is shown in Fig. 6(a).

TABLE II. Average geometry of oxidized  $\text{Si}_x$  nanocrystal samples.

|           | Diameter ( $\text{\AA}$ ) |                     |                    | Thickness ( $\text{\AA}$ ) |                |
|-----------|---------------------------|---------------------|--------------------|----------------------------|----------------|
|           | $D_{\text{outer}}$        | $D_{\text{middle}}$ | $D_{\text{inner}}$ | $\text{SiO}_x$             | $\text{SiO}_2$ |
| <i>vs</i> | $26 \pm 6$                | 14                  | 11                 | 1.5                        | 6              |
| <i>s</i>  | $33 \pm 6$                | 21                  | 17                 | 2                          | 6              |
| <i>m</i>  | $45 \pm 7$                | 34                  | 31                 | 1.5                        | 5.5            |
| <i>l</i>  | $96 \pm 19$               | 81                  | 78                 | 1.5                        | 7.5            |

### O-passivated Si nanocrystals

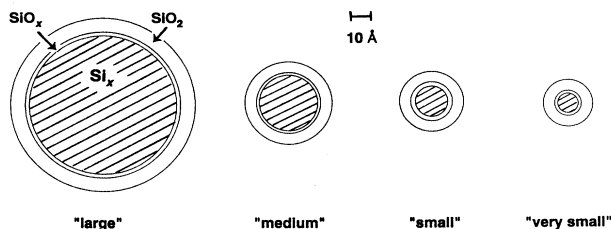


FIG. 4. Schematic illustration of different oxidized Si nanocrystals, drawn to relative scale. Numerical values of average inner- $\text{Si}_x$ -core diameters and of average outer- $\text{SiO}_2$ - and interfacial- $\text{SiO}_x$ -layer thicknesses are given in Table II.

The por-Si film is laterally nonuniform with a maximum thickness of  $8 \mu\text{m}$ . The porous material occurs within  $\lesssim 5\text{-}\mu\text{m}$ -thick irregular cylinders having hemispherical ends. Between these cylinders of porous material are  $< 0.5\text{-}\mu\text{m}$ -thick pillars of unetched Si, some of which extend up to the specimen surface. The average thicknesses of the porous layers in samples *C* and *A* are very different, about 6 and  $70 \mu\text{m}$ , respectively, but both samples also contain similar porous cylinders. The top  $\sim 0.5 \mu\text{m}$  of the films in samples *B* and *C* appear somewhat more dense than the bulk of the film, whereas no difference in surface layer is observed in sample *A*.

Within the porous region of samples *A*, *B*, and *C* we observe granular features  $\sim 30\text{--}60 \text{\AA}$  in diameter; see Fig. 6(b). This characteristic size is, of course, a maximum dimension for any single crystallite. When viewed perpendicularly to the growth direction, these features appear to be aligned in irregular columns. Dimensions on the scale of a few nm have been reported in TEM stud-

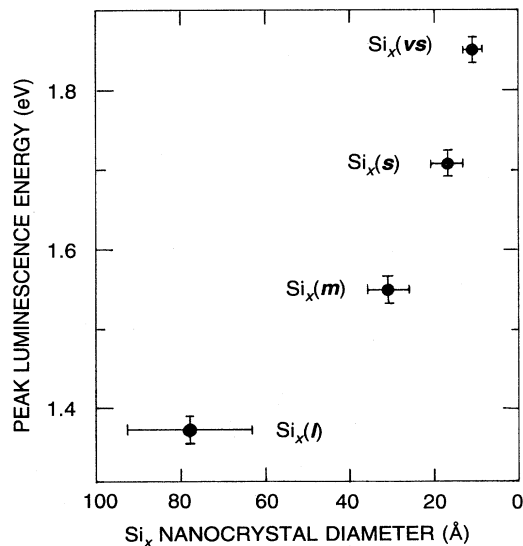


FIG. 5. Peak photoluminescence energy vs average diameter of inner  $\text{Si}_x$  cores in very small (*vs*), small (*s*), medium (*m*), and large (*l*) oxidized Si nanocrystal samples. Error bars mainly reflect the size distribution of particles.

ies<sup>13–16,22,23</sup> of por-Si formed from high-resistivity *p*-type Si,<sup>79</sup> although the granular structures described here are typically observed only in specimens prepared without ion milling.<sup>16,24,65,80,81</sup> At high resolution, some small (<50 Å) regions of lattice planes can be seen which are slightly misaligned with respect to the substrate orientation. Most of the sample, however, does not show lattice fringes. From the images it is not possible to determine whether this is a result of crystallites being misoriented too far from a diffracting condition, or from the sample itself being amorphous.

Consistent with other observations,<sup>16,80</sup> the diffraction pattern shows weak Si reflections that are diffuse and spread into arcs, implying a mosaic spread in the crystallites exceeding 20°. In our specimens, the reflections are superposed on a strong background of amorphous rings. Quantifying the fractional amount of crystalline material, particularly in the near-surface region of the layers, is

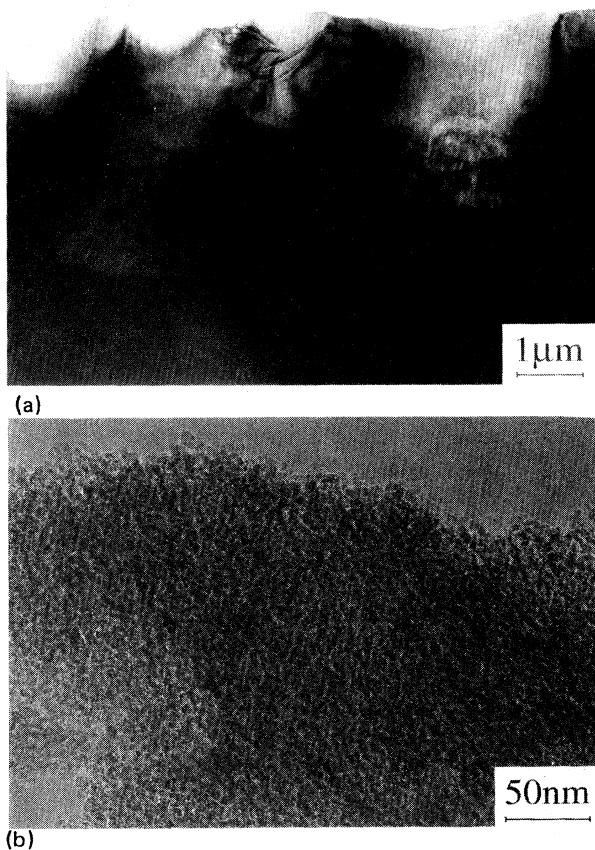


FIG. 6. (a) Large-scale structure of por-Si (*B*), obtained with bright-field (110) image of an ion-milled cross-sectional specimen. The porous material, seen within two well-defined cylindrical regions, shows a mottled contrast. Apart from the overall film thickness, por-Si (*A*) and por-Si (*C*) samples appear similar at this magnification. (b) Small-scale structure of por-Si (*C*). The porous region is composed of granular features with 30–60-Å characteristic sizes. There is some variability in the feature size at different parts of the layer. por-Si (*A*) and por-Si (*B*) samples appear identical in the TEM micrographs.

complicated by the unknown amount of unetched Si in this region, the unknown degree of oxidation of the specimen prior to TEM examination, and the possibility of additional oxidation induced by the electron beam itself.<sup>82</sup>

Sample *D*, described elsewhere,<sup>65</sup> is very different from the other three samples. This porous film is free standing, about 18 μm thick, highly uniform, and exhibits no large-scale structures. Average characteristic features of about 60 Å are observed in phase-contrast TEM micrographs.

It is important to remember that most of the structural features characterized in the TEM images are observed at depths far exceeding the <0.5-μm near-surface region from which the visible luminescence originates.<sup>32</sup> A method more closely matched to this near-surface length scale is x-ray absorption detected with total electron yield.<sup>50</sup> The *extended* region of the absorption data is used to characterize the *geometric* structural properties of the por-Si samples, and this is discussed in Sec. III B 2. Here we focus on the *near-edge* region of the data, which we have seen above for the Si nanocrystals can provide *electronic* structural information about the por-Si layers, i.e., chemical composition. Normalized NEXAFS data from freshly prepared por-Si samples appear in Fig. 2(b), along with comparison data from *c*-Si and HF-rinsed *a*-Si. For clarity, we show only two of the four samples studied, labeled *B* and *C* (*A* is similar to *B*, and *D* is similar to *c*-Si). Qualitatively, there is closer resemblance of the por-Si data to that of *c*-Si rather than to *a*-Si. Also, as noted elsewhere,<sup>49</sup> there is a conspicuous lack of (Si-O)-related absorption at ~1842–1848 eV in the por-Si samples.

The absence of a Si-O species in the NEXAFS data can be misleading for ruling out its possible importance in the luminescence in por-Si. As will be shown in Sec. III B 2, even freshly prepared anodically grown por-Si samples, which have been minimally exposed to air and quickly inserted into high vacuum, still contain residual oxygen in the form of physisorbed ethanol trapped on the internal surfaces of the porous material. This oxygen goes undetected in the Si *K*-edge NEXAFS data because the samples from which the x-ray-absorption data are measured have not been exposed to photoexciting radiation, i.e., the oxygen remains in the form of unreacted ethanol. By contrast, the photoluminescence measurements necessarily involve exciting radiation, which could photodissociate the ethanol and lead to the formation of one of several forms of Si-O species. That this reaction process of photoinduced oxidation *can* occur is not the issue;<sup>29,30</sup> rather, it is whether any so-generated Si-O species is at all related to the observed visible photoluminescence in por-Si.

We have investigated this point using transmission ir-absorption measurements to monitor the dependence of photo-oxidation as a function of radiation exposure. The top of Fig. 7 shows transmission data from the two nonirradiated por-Si samples in Fig. 2(b), namely *B* and *C*. These raw transmission spectra reflect features in source intensity, interferometer efficiency, mirror absorption, and detector response. The bottom traces are *difference* spectra from those samples before and after exposure to 4

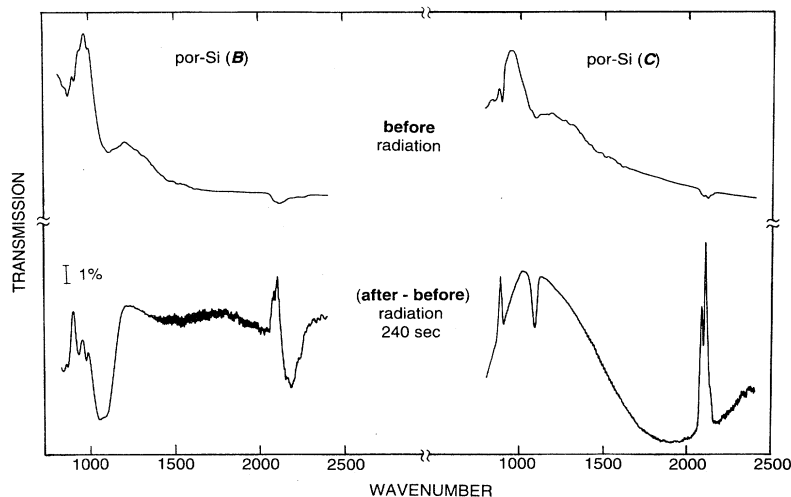


FIG. 7. Infrared-absorption data from two differently prepared por-Si samples. Photoinduced oxidation (arising from exposure of H-passivated por-Si surfaces to 390-nm radiation) is evident in difference spectra (bottom traces) by the appearance of Si-O absorption at  $\sim 1100\text{ cm}^{-1}$  and a corresponding decrease of Si-H absorption at  $\sim 2100\text{ cm}^{-1}$ .

min of 390-nm exciting radiation, conditions very similar to those used in our photoluminescence measurements. In both samples there is enhanced absorption around  $1100\text{ cm}^{-1}$ , representative of Si-O-Si stretching frequencies,<sup>83</sup> and a loss of absorption around  $2100$  and  $900\text{ cm}^{-1}$ , representative of Si-H<sub>x</sub> stretching and Si-H<sub>2</sub> scissor frequencies.<sup>84</sup> The loss of hydrogen is roughly 10% of the total amount in the sample. Since the photoexciting radiation only penetrates  $\sim 0.5\text{ }\mu\text{m}$ , which is also about 10% of the total por-Si layer ( $\sim 5\text{--}8\text{ }\mu\text{m}$ ), this suggests that a large fraction of the H may be removed within the near-surface region either by direct Si-H photodissociation, by reaction with O, or by both. The increase of oxygen bound to Si is less easily quantified. Sample B shows an uptake of oxygen in the backbones of H-terminated Si, seen by the increased absorption at  $\sim 2200\text{ cm}^{-1}$ . The oxide region at  $800\text{--}1200\text{ cm}^{-1}$  also exhibits many different features, suggesting multiple oxygen-bonding configurations. By contrast, sample C loses H and essentially forms a single Si-O-Si species. Clearly, photo-oxidation occurs in both samples.

We use the simpler ir absorption spectra in sample C to study the consequences of this effect. Expanded views of the two regions in the por-Si (C) sample are shown in Fig. 8 for different radiation exposure times. The data were obtained by translating a wafer with separate portions exposed for different amounts of time. A clear monotonic trend with exposure is observed for the Si-O and Si-H species (this trend saturates after  $\sim 100\text{ s}$ ). Significantly, however, the luminescence peak intensities and energies both remain *constant* with radiation exposure.<sup>85</sup> This straightforward result directly demonstrates that despite the occurrence of photo-oxidation, there is *no* correlation between the photo-oxidized species and the observed photoluminescence in the visible region. Along with the NEXAFS data in Fig. 2(b), our results collectively rule out the importance of an oxygen-containing component in por-Si, either incorporated as part of the surface layer,<sup>51–53</sup> as a defect,<sup>56–58</sup> or as a Si<sub>x</sub>O<sub>y</sub>H<sub>z</sub> molecule.<sup>30,54,55</sup>

## 2. EXAFS, FRS, ir absorption, and luminescence data

Having established the overall structure of the por-Si films, the chemical composition of the near-surface layers prior to radiation exposure, and the fact that after exposure the visible luminescence properties are not related to an O-containing species, we obtain more detailed structural information using extended x-ray-absorption fine-structure (EXAFS) measurements.<sup>50</sup> Figure 9(a) displays the raw x-ray-absorption data from por-Si (B), por-Si (C), c-Si, and a-Si, i.e., the same systems in which only the near-edge region was shown [Fig. 2(b)]. As the

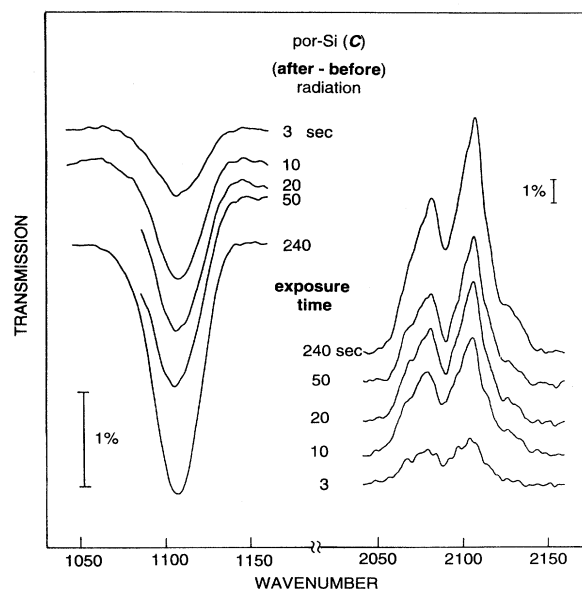


FIG. 8. Infrared-absorption difference spectra from a por-Si (C) sample showing a growth in Si-O absorption and a loss in Si-H absorption, both as a function of exposure time to 390-nm photoexciting radiation.

acronym EXAFS implies, the fine structure extends several hundreds of eV above the absorption edge. Relative to *c*-Si, such extended structure is less intense and less complex for the por-Si and *a*-Si samples. The EXAFS,  $\chi(k)$ , is analyzed following standard procedures,<sup>50</sup> namely truncating the data above the edge, removing the smooth (essentially atomic) background, and converting from photoelectron energy space into photoelectron momentum ( $k$ ) space, weighted by  $k^2$ . The raw,

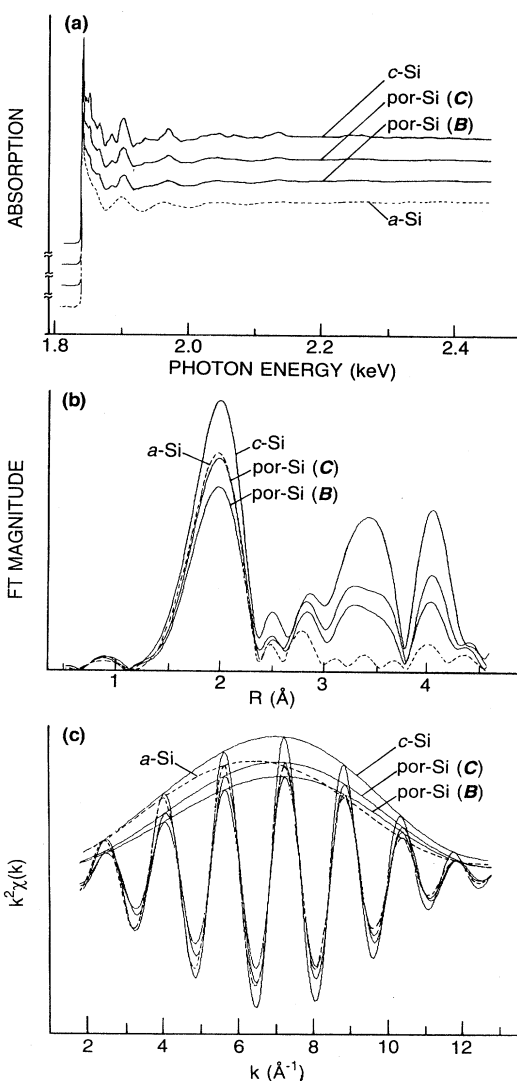


FIG. 9. (a) Raw Si *K*-edge EXAFS data from *c*-Si, *a*-Si, and two differently prepared por-Si samples. (b) Fourier transforms of edge-truncated,  $k^2$ -multiplied, background-subtracted data from samples in (a). First-, second-, and third-shell peaks at  $\sim 2.0$ ,  $3.4$ , and  $4.1$  Å are uncorrected for the phase shift. Artifactual peaks at  $\sim 2.5$  and  $2.9$  Å are due to truncation. (c) Back-transformed, filtered first-shell data from (b). Average first-shell Si-Si bond lengths, obtained from the frequency of the EXAFS, are identical in all four systems, but the average first-shell Si coordination  $\bar{N}_{\text{Si}}$ , obtained from the amplitude function enveloping the EXAFS, is larger in *c*-Si than in the por-Si samples.

background-subtracted data are then Fourier transformed (FT) into distance ( $R$ ) space to isolate and identify the different nearest-neighbor shells around the absorbing Si atom. The results are shown in Fig. 9(b). The first three FT peaks, corresponding to the first three Si coordination shells, appear at approximate distances (uncorrected for scattering phase shifts) of  $2.0$ ,  $3.4$ , and  $4.1$  Å. The smaller peaks in the transform correspond to a combination of residual background, noise, and truncation errors. The second- and third-shell peaks are most intense in *c*-Si, and are still evident in the por-Si samples. Such peaks are essentially absent in *a*-Si due to static disorder, i.e., the short-range disorder of the slightly different second- and third-shell Si-Si distances lead to destructive interference of their corresponding EXAFS. The first-neighbor FT peaks in all four samples appear at the same value of  $R$ . Only their amplitudes are different.

To gain insight into these amplitude differences, we isolate the first-neighbor EXAFS from that of the higher shells by placing a filter (i.e., window function) around the  $\sim 2$ -Å FT peak and then backtransforming into  $k$  space. The filtered first-shell data are shown in Fig. 9(c), along with the corresponding amplitude functions  $A(k)$  that envelope the oscillatory EXAFS. Relative to that in bulk *c*-Si, the peak intensity of  $A(k)$  in *a*-Si is shifted to lower  $k$  as a result of the Debye-Waller-like static-disorder term,  $\exp(-2k^2\sigma^2)$ , where  $\sigma$  is an effective rms displacement.<sup>50</sup> Such exponential damping is important at high  $k$  and less so for  $k < 4$  Å<sup>-1</sup>, so in the low- $k$  region for the *a*-Si and *c*-Si samples  $A(k)$  is the same. This reflects their identical first-neighbor Si coordinations of 4. By contrast, the peak intensities of the amplitude functions in the por-Si samples are *unshifted* relative to that in *c*-Si. In fact, in these samples  $A(k)$  is *smaller* at *all* values of  $k$ . This is an obvious indication that in por-Si the *average* coordination of Si atoms,  $\bar{N}_{\text{Si}}$ , i.e., the number of first-neighbor Si-Si bonds per total number of Si atoms, is less than 4.

The reason for this lower average Si coordination number and the apparent lack of other first neighbors in the FT data of por-Si is that the surface Si atoms are also coordinated to H. Since the EXAFS backscattering amplitude of H is negligible, it appears that the photoabsorbing Si atoms are less than fourfold coordinated; in actual fact, the “missing” Si nearest neighbors are H atoms. Least-squares fitting the filtered por-Si data in Fig. 9 over the entire  $k$  range yields substantially smaller values of  $\bar{N}_{\text{Si}}$ . In sample *B*, for example,  $\bar{N}_{\text{Si}} = 2.86 \pm 0.1$ .

To get an idea of how significant this effect is in the por-Si samples, consider the hypothetical cluster shown in Fig. 10 consisting of 14 Si atoms passivated with enough H atoms, in this case 24, to saturate all the Si dangling bonds. There are four bulk Si atoms with  $N_{\text{Si}} = 4$ , six surface Si atoms with  $N_{\text{Si}} = 2$ , and four surface Si atoms with  $N_{\text{Si}} = 1$ , giving a total of 32 Si-Si bonds for an average Si coordination  $\bar{N}_{\text{Si}} = 32/14 = 2.29$ . The average number of missing Si-Si bonds is  $4 - 2.29 = 1.71$ , which is, of course, just the average H-atom coordination  $\bar{N}_{\text{H}}$  (six dihydride Si atoms with  $N_{\text{H}} = 2$  and four trihydride Si atoms with  $N_{\text{H}} = 3$ , or 24 total H atoms). Alternatively, we can say that in the  $\text{Si}_{14}\text{H}_{24}$  cluster, the H/Si

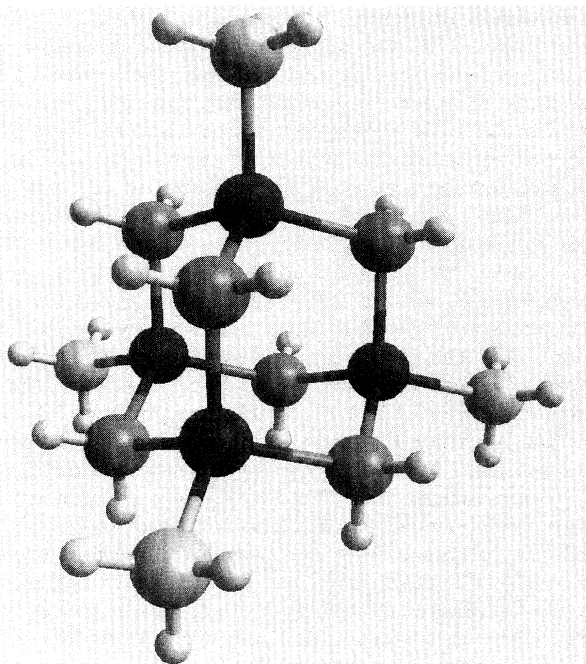


FIG. 10. Hypothetical  $\text{Si}_{14}\text{H}_{32}$  cluster/molecule. Darkest spheres are (bulk) Si atoms coordinated to the other four Si atoms, and lighter spheres are (surface) Si atoms coordinated to either two or three H atoms, which are represented by the smaller, lightest spheres. In this  $\approx 8\text{-\AA}$  cluster, the average Si coordination  $\bar{N}_{\text{Si}}$  is 2.29, and the H/Si ratio is 1.71.

ratio is 1.71. Now, in sample *B*, we obtained a value of  $\bar{N}_{\text{Si}} = 2.86 \pm 0.1$ , which means  $\text{H/Si} = 1.14 \pm 0.1$ , or an average H content in that sample of 114%. This result is striking not only when compared with such a small  $\text{Si}_{14}\text{H}_{24}$  cluster of  $\approx 8\text{ \AA}$ , but when compared with typical "high" concentrations of H,  $\sim 10\%$ , in actual device-quality *a*-Si:H.<sup>88</sup>

The small average Si sizes implied by the EXAFS data are so small, in fact, that before discussing their implications it is important to confirm their reliability with independent experiments. Our discussion above suggests that we should be able to check our EXAFS-determined  $\bar{N}_{\text{Si}}$  values by measuring the H/Si ratios in the corresponding samples. Figure 11 shows FRS data from samples *B*, *C*, and *D*. The left-hand vertical scale plots the number of recoil H counts/channel, which is nearly proportional to the H/Si ratio given on the right. The upper horizontal axis plots the energy of the H atoms reaching the detector after having passed through the mylar-foil filter. Because H atoms closest to the surface are recoiled with the highest energy, this axis is a reversed sampling-depth scale.<sup>89</sup> Converting this depth, which is directly expressible in Si atoms per  $\text{cm}^2$ , to an effective length scale in the por-Si material involves knowing its density. We have assumed, for simplicity, that all the samples studied have 80% porosities, i.e., densities 20% of bulk Si, and this is reflected in the lower horizontal scale. Inspection of the total effective thickness of the H-containing layers in the por-Si samples shows them to be  $> 3\text{ }\mu\text{m}$  (in agreement with the TEM results), substantially larger

than the near-surface sampling depth in the luminescence and x-ray-absorption measurements,  $\approx 0.5\text{ }\mu\text{m}$ .

The approximate boundary of the near-surface region of interest is indicated by the dashed vertical line at  $0.5\text{ }\mu\text{m}$ . Within this region, the H concentration changes slowly with depth, showing that the relevant results are actually insensitive to our assumed porosity values. From Fig. 11, the H/Si ratios in the near-surface region are measured to be 1.20, 0.80, and 0.42 for samples *B*, *C*, and *D*, respectively. The uncertainties in these values are  $\approx 10\%$ , determined by statistics. The data shown were taken with very low doses of incident  $\text{He}^+$  ions because it was found that extended  $\text{He}^+$  bombardment reduces the H concentration. Extrapolation to a zero incident  $\text{He}^+$  dose, based on a series of low-dose bombardments, gives correspondingly adjusted H/Si ratios of 1.25, 0.83, and 0.44. These results are somewhat larger but still consistent with those inferred from EXAFS, namely 1.14, 0.76, and 0.33, respectively.

The fact that the FRS measurements probe all the H in the sample as a function of depth and that they cannot

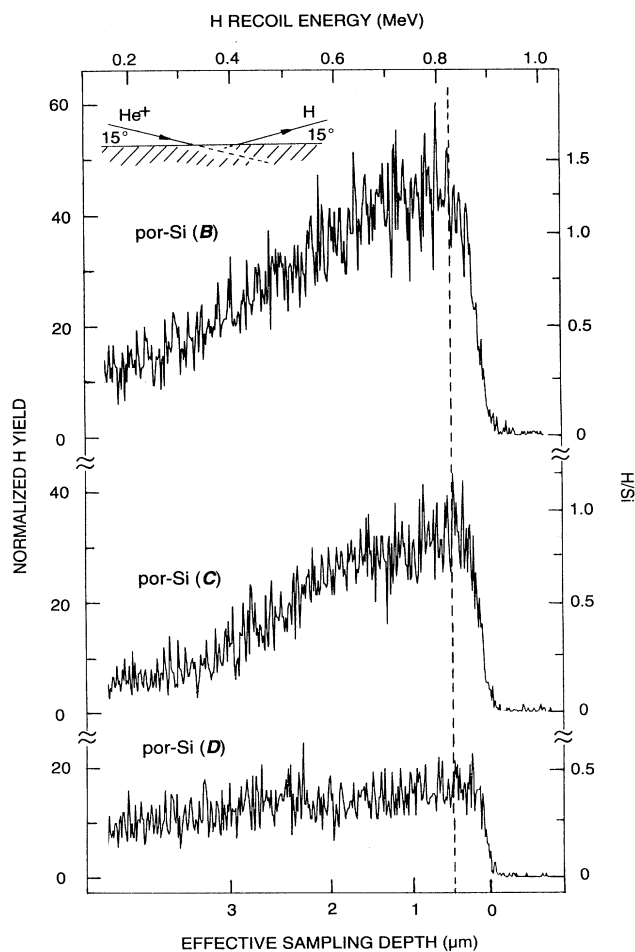


FIG. 11. FRS data for directly determining H/Si ratios as a function of depth from three differently prepared por-Si samples. The dashed vertical line at  $0.5\text{ }\mu\text{m}$  is drawn to define the approximate boundary of the optically relevant near-surface region.

discriminate between H atoms in different chemical environments invites additional characterization using ir-absorption spectroscopy. Figure 12 displays ir-absorption spectra from sample *B* recorded in transmission- and grazing-incidence configurations. The transmission spectrum (dashed line) shows a broad H-related contribution centered at  $\sim 2100 \text{ cm}^{-1}$  with three features, similar to ir data reported earlier.<sup>29,90</sup> The features correspond to H directly bound to Si in the form of monohydrides ( $2070\text{--}2085 \text{ cm}^{-1}$ ), dihydrides ( $2090\text{--}2115 \text{ cm}^{-1}$ ), and trihydrides ( $2130\text{--}2140 \text{ cm}^{-1}$ ).<sup>83</sup> Weak structures between  $\sim 2180$  and  $2280 \text{ cm}^{-1}$ , corresponding to H in H-Si-O,<sup>84</sup> arise from the  $> 10$ -min exposure in air of this particular sample (see below). There is no O-H stretch absorption at  $\sim 3300 \text{ cm}^{-1}$  arising from water, but there are weak contributions from C-O and C-C stretches and from  $\text{CH}_x$ -stretch and -deformation modes characteristic of physisorbed ethanol.

The grazing-incidence data (solid line) is dramatically different.<sup>91</sup> The dominant H-Si peak is now centered at  $\sim 2130 \text{ cm}^{-1}$ , with very small monohydride absorption at  $2080 \text{ cm}^{-1}$ . The greater surface sensitivity of the grazing-incidence configuration (see Sec. II F) is most evident by the relatively larger absorption from the H-Si-O component in this sample. (Other samples with air exposure  $< 10$  min showed essentially no absorption from this component, but with increasing air exposure its intensity grew at the expense of H-Si absorption.) This fact, along with the observation of weak H-O and H-C absorption from ethanol and no H-O absorption from water, indicates that the H probed in the optically relevant near-surface region originates predominantly from H-Si bonds. FRS measurements from the same near-surface region, therefore, do indeed largely represent H atoms directly bound to Si, thereby validating the EXAFS determinations of  $\bar{N}_{\text{Si}}$  and the correspondingly inferred H/Si ratios. The grazing-incidence ir data also show that in the near-surface region the H atoms exist mainly in the form of

dihydride and trihydride surface terminations. Finally, the weak absorption from ethanol, which is not removed with vacuum pumping, identifies ethanol (rather than water) as the physisorbed species that undergoes photodissociation. The ethanol is an additional, albeit minor, source of H not directly bound to Si prior to photoexcitation, consistent with the slightly higher H/Si ratios measured by FRS relative to those inferred from EXAFS.

The por-Si samples exhibit not only very large and different H/Si ratios, but also different luminescent properties. In Fig. 13, as a function of  $\bar{N}_{\text{Si}}$ , we plot the peak energies in the luminescence spectra from the four por-Si samples (typical luminescence data have already been reported<sup>24,49,65</sup>). A well-defined trend is observed, reminiscent of that found in Fig. 5 for the different sizes of the Si nanocrystals. This suggests that  $\bar{N}_{\text{Si}}$  and the effective size of the optically active species in por-Si are directly related, a correlation that is explored in Sec. IV.

#### IV. DISCUSSION

We have seen that the peak luminescence energy measured in a por-Si sample varies with the EXAFS-measured average Si-Si coordination,  $\bar{N}_{\text{Si}}$ , and that this latter value reflects the amount of H coordinated to Si atoms at the internal surfaces of por-Si. Thus, a small  $\bar{N}_{\text{Si}}$  means a large H/Si ratio, which in turn implies a large average surface/volume ( $S/V$ ) ratio—i.e., a small size—for the representative Si structure(s) in that sample. The actual size of the structure can be inferred once its shape is known.

In Fig. 14, values of  $\bar{N}_{\text{Si}}$  are calculated for different shapes and plotted as a function of inverse characteristic dimension, or inverse “length.” This length corresponds to the diameter for a sphere, or the side for a cube or rhombus. Square-prism shapes with aspect ratios of 4:1:1 are included to represent prolate particles. All particle or

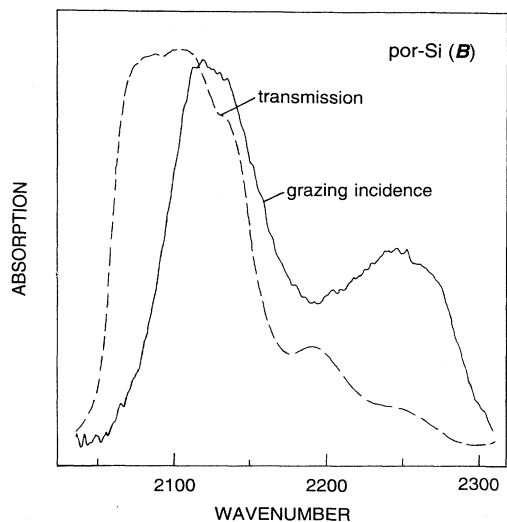


FIG. 12. Infrared-absorption data from a por-Si (*B*) sample in transmission vs grazing-incidence configurations (see Fig. 1).

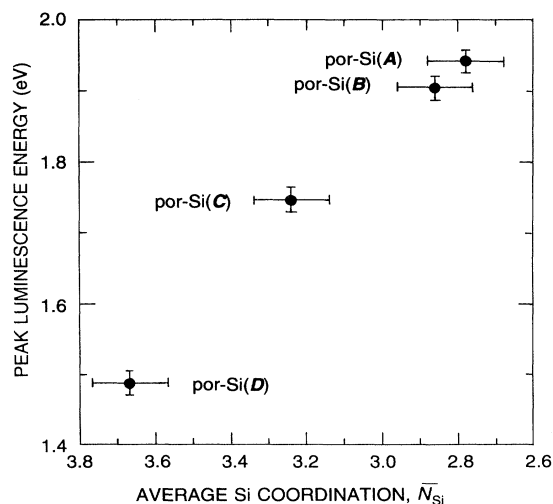


FIG. 13. Peak luminescence energy vs average Si coordination,  $\bar{N}_{\text{Si}}$ , determined from EXAFS data of four differently prepared por-Si samples.

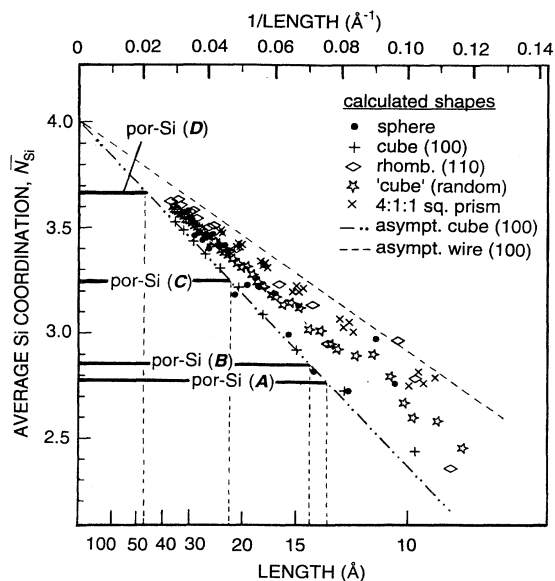


FIG. 14. Correlation between average Si coordination calculated for particles of different shapes vs their inverse characteristic length (diameter for sphere; side for cube, rhombus, or wire). The average includes bulk and surface atoms, which have less than four first neighbors, explaining the trend of lower values with decreasing particle size. Experimental Si coordinations from EXAFS data of four differently prepared por-Si samples are indicated, as are upper-limit characteristic lengths.

wire surfaces are terminated with H and are ideal. For the cases of (100)-faceted cubic particles and (100)-faceted square wires, dot-dashed and short-dashed lines are drawn from the asymptotic value of  $\bar{N}_{\text{Si}} = 4.0$  (representing infinitely large crystal sizes) and extrapolated to smaller dimensions. These asymptotic lines effectively bracket the calculated  $\bar{N}_{\text{Si}}$  values of the other shapes considered, thereby establishing upper and lower limits of size for most other structures.<sup>92</sup> For undulating or constricted wire shapes, which have been suggested,<sup>16,34,93</sup> recent theoretical work<sup>62</sup> finds that their properties fall on the same lower-limit (dashed) line shown for the smooth wire shape. As an aside, it is interesting to note that the spheres lie almost on the same upper-limit (dot-dashed) line as the (100) cubes because, for a given diameter or side, their  $S/V$  ratios are (perhaps nonintuitively) almost identical.<sup>94</sup>

Using the calculated plot in Fig. 14, we now consider the  $\bar{N}_{\text{Si}}$  values measured from the EXAFS amplitudes in the four different por-Si samples. Upper limits for the average size of the Si structures are obtained from the intersection of the corresponding experimental  $\bar{N}_{\text{Si}}$  values with the asymptotic dot-dashed line for (100) cubes. Taking into account the  $\pm 0.1$  uncertainties in  $\bar{N}_{\text{Si}}$ , which were omitted in Fig. 14 for clarity, we obtain mean upper-limit Si sizes of  $49^{+21}_{-11}$ ,  $21.4^{+3.3}_{-2.5}$ ,  $14.3^{+1.4}_{-1.2}$ , and  $13.4^{+1.2}_{-1.0}$  Å for samples D, C, B, and A, respectively. In a similar manner, for simplicity we take the mean lower-limit sizes as those determined from the asymptotic dashed line for (100) wires, giving corresponding values of  $33^{+14}_{-8}$ ,  $4.3^{+2.2}_{-1.7}$ ,  $9.5^{+0.9}_{-0.8}$  and  $8.9^{+0.8}_{-0.6}$  Å.

As small as these mean upper- and lower-limit sizes are for the average structures in por-Si, the *actual* limiting sizes in these samples are even smaller. Recall that the experimentally quoted  $\bar{N}_{\text{Si}}$  values reflect an average Si coordination for *all* Si atoms in the near-surface region, and that the TEM micrographs showed macroscopic portions of unetched *c*-Si in samples A, B, and C. This means that the quoted  $\bar{N}_{\text{Si}}$  values for these samples include Si atoms not only in por-Si but in some fraction of unetched *c*-Si where the Si coordination is the maximum value of 4. Accordingly, the actual values of  $\bar{N}_{\text{Si}}$  representing por-Si alone must be smaller than those quoted. As stated in Sec. III B 1, it is difficult to quantify the amount of *c*-Si in the por-Si samples (estimates vary between 10% and 20%, depending on the sample), so we have chosen to leave our results uncorrected. It is worth noting, however, that even after subtracting 10–20% of *c*-Si from the raw por-Si EXAFS spectra and analyzing the results as in Fig. 9, clear signs of second- and third-neighbor shells in the FT data still persist. Therefore, the *local* structure of por-Si is *crystalline*, not amorphous, as might be inferred in measurements more sensitive to long-range order, e.g., TEM and diffraction.

In the bottom of Fig. 15, we plot with squares the mean peak luminescence energies for the por-Si samples against the inverse of their mean upper-limit sizes. Also included in the top half of the figure is a simplified version of Fig. 14, to serve as reference for determining the (uncorrected) lower-limit sizes from the dashed line for (100) wires. Finally, plotted with circles in the bottom half are the peak luminescence energies for the  $\text{Si}_x$  nanocrystalline samples. The trends for the two very different types of  $\text{Si}_x$  and por-Si samples are remarkably similar. Indeed, had we corrected the upper-limit sizes by excluding  $\sim 10\%$  contributions of *c*-Si to the quoted  $\bar{N}_{\text{Si}}$  values for por-Si, the trends would be virtually the same.

The implication of the similar trends is clear: Since the luminescence spectrum for a given  $\text{Si}_x$  nanocrystalline particle is directly correlated with its size, the luminescence spectrum from a given por-Si sample is also associated with a characteristic Si size. Thus, for example, the observation of peak luminescence at 710 nm for *any* freshly prepared (uncontaminated) por-Si sample implies that such luminescence is representative of a Si structure, or set of structures, whose average dimension is  $\lesssim 22$  Å. It is unimportant whether or not the por-Si sample in question is heterogeneous, containing smaller or larger Si particles or even macroscopic regions of unetched *c*-Si, or that its internal surface is passivated with H or with a photo-oxidized species. The reason is that the EXAFS-determined  $\bar{N}_{\text{Si}}$  values which establish the trend in Fig. 15 are, by definition, mass-weighted *average structural* quantities of the por-Si sample probed over the entire near-surface measurement region. In other words, the  $\bar{N}_{\text{Si}}$  values are *not* representative of some minority species. That the size-weighted *average optical* quantities being measured—that is, the peak luminescence energies—are also *not* representative of some minority species from por-Si is based on the very similar dependence of size versus peak luminescence energy found for the  $\text{Si}_x$  inner cores, whose composition and structure

determined here and whose detailed luminescence properties characterized elsewhere<sup>78</sup> have indeed identified them as the *dominant* optically active species.

Figure 15 provides information about the average shape, as well as size, of the Si structures associated with peak luminescence energies in the visible region, i.e.,  $< 700$  nm ( $> 1.75$  eV). The two por-Si samples in this work that are relevant to this region are *B* and *A*. Their mean *upper-limit* sizes, corresponding to (100)-cubic- or spherical-shaped particles, are  $\sim 14$  and  $\sim 13$  Å, respectively. These dimensions are below the  $\sim 20$ -Å detection limit observable with TEM or diffraction. If these por-Si samples were assumed to be predominantly composed of

particles whose shapes were different from spheres or (100) cubes, their average size would have to be even smaller. The mean *lower-limit* sizes, which we have taken to correspond to (100)-wire shapes, are  $\sim 9.5$  and  $\sim 8.9$  Å for samples *B* and *A*, respectively. Such small sizes are comparable to that of the hypothetical  $\text{Si}_{14}\text{H}_{32}$  cluster shown in Fig. 10. Moreover, as mentioned above, the actual lower-limit sizes are smaller still because the quoted  $\bar{N}_{\text{Si}}$  values are uncorrected for the *c*-Si contribution. Based on such unphysically small sizes for wire structures which would have to represent the *majority* of the por-Si sample (otherwise the values would not be average quantities), we conclude that locally crystalline Si *particles* rather than wires are the dominant shapes of the species responsible for the visible luminescence.<sup>11,61</sup> This conclusion cannot be extended to por-Si samples whose peak luminescence falls in the near- and far-infrared regions, i.e.,  $> 700$  nm, because the distinction between particles and wires in Fig. 15 is less significant.

The above conclusions lead to an apparent disagreement with earlier results<sup>8,16</sup> for por-Si samples prepared very similarly to our sample *C*. Those TEM and luminescence studies report wirelike structures of  $\approx 20$  Å and luminescence that is clearly visible and bright. Without focusing on whether or not the shapes of the structures are predominantly wirelike, the average characteristic size reported for those structures is indeed consistent with our own findings. What is not consistent is that the *peak* luminescence wavelength observed by us for sample *C* occurs at  $\sim 710$  nm, beyond the range of visible detection. This discrepancy can be reconciled, however, by recognizing that only the shorter-wavelength *tail* of the luminescence spectrum for this sample falls in the spectrally sensitive visible range of the human eye. Thus it appears that it is an optical minority species (equivalently corresponding to a structural minority species of smaller size, as shown in this work), which is responsible for the visible luminescence in such *C*-like samples whose structures are of larger average (i.e., majority) size.

A similar discrepancy for larger-size structures is seen in the luminescence of the ox-Si<sub>x</sub>(*l*) nanocrystalline sample, whose average crystalline Si core is about 80 Å. The peak luminescence for this sample is observed at 900 nm with a full width at half maximum of 200 nm. An 80-Å particle, however, should have a band gap and corresponding luminescence wavelength very close to the bulk value of 1060 nm. As in the case of the larger average-sized structures in some por-Si samples, the observed emission at shorter wavelengths is traceable to the fraction of smaller-sized particles, i.e., a minority species, with relative higher luminescence yields. This problem is not encountered in samples of smaller average dimensions because their size distributions are much narrower.

While on the subject of apparent disagreements with previous work, it is important to note that our conclusions about the structural and compositional properties of the visible-light-emitting species apply only to freshly prepared por-Si samples that have undergone minimal exposure to air. Exposure to photoexciting radiation is obviously unavoidable in luminescence measurements, but we have shown that the photo-oxidized

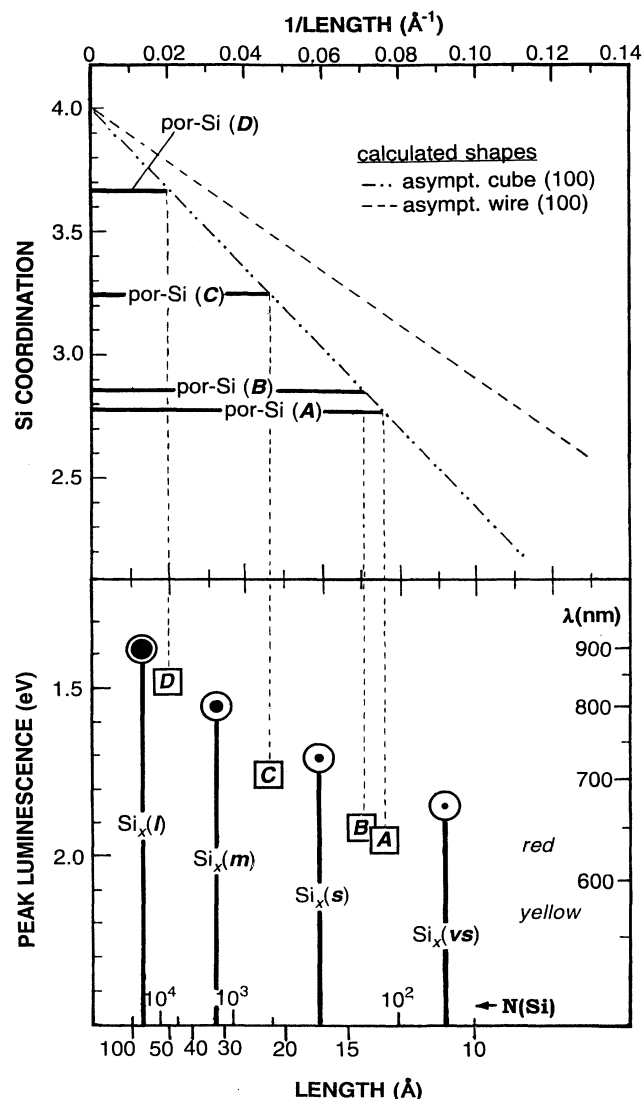


FIG. 15. Correlation between the average characteristic length of a Si structure and its measured peak luminescence energy. Also indicated are the total number of Si atoms,  $N(\text{Si})$ , contained in a cubic particle of corresponding length. Different sizes of the oxidized Si nanocrystals, shown as circles, are from Fig. 5. Different sizes from the por-Si samples, shown as squares, are upper-limit values from Fig. 14, a simplified version of which is reproduced at the top.

species in our samples do not measurably affect the observed visible luminescent properties.<sup>85</sup> Our conclusions do not imply that samples exposed to air or exciting radiation for extended periods of time or prepared in ways very differently than those described here could not exhibit different luminescent properties or features characteristic of some oxygen-containing species. What we are saying is that in por-Si samples prepared by methods common to a wide variety of other workers and handled with reasonable care, the *dominant* optically active species are structures whose *surfaces are passivated* (with H or O, or both) but whose *cores* are composed only of *locally crystalline* Si.

The actual number of Si atoms  $N(\text{Si})$  contained within the characteristic por-Si structures, which are responsible for the visible luminescence, is small. The particular  $N(\text{Si})$  value depends, of course, on the shape of the structure. In the bottom of Fig. 15 we have indicated  $N(\text{Si})$  values for (100)-cubic particles, which happens to be the maximum number of Si atoms for any particle of a given characteristic size.<sup>95</sup> Combining this information with our other results, it is possible to envision a generic por-Si structure whose average shape and size are associated with peak visible emission. Figure 16 shows such a model for an average  $\sim 13\text{-}\text{\AA}$  structure typifying a sample similar to por-Si (A). It is a nearly rectangular particle of 86 Si atoms, a number less than the maximum of  $\sim 110$  atoms for a (100)-faceted cube of this size but more than the  $\sim 60$  atoms for a sphere<sup>95</sup> of the same characteristic dimension. The passivating surface H atoms have been omitted for clarity. Consistent with our x-ray- and ir-absorption results on the expected relative number and type of Si surface atoms, 31 of the 51 such atoms are dihydride species on (100)-like surfaces; the remaining 11

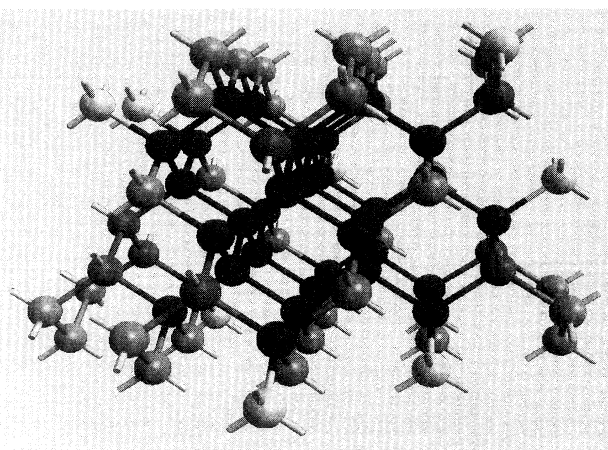


FIG. 16. A typical visible-light-emitting por-Si structure. Its characteristic size is about  $13\text{ \AA}$  and its shape is approximately rectangular with predominantly (100) surfaces. All dangling bonds of surface Si atoms, shown unpassivated, are presumed passivated mainly with H atoms in freshly prepared material (some bonds must obviously be connected to other Si atoms of adjacent por-Si structures in an actual sample). Of the 86 Si atoms, only 35 (dark) are bulklike, with a Si coordination of 4. The average Si coordination in this structure is 2.79, very similar to that measured in the por-Si (A) sample.

trihydride and 9 monohydride species lead to an average Si coordination in the particle of  $\bar{N}_{\text{Si}} = 2.79$ . While this is only a model which ignores, among other details, how the particle is interconnected with the other Si structures in the por-Si film, it does offer a simple visualization of the very small size and approximate shape of the visible-light-emitting particles in a typical por-Si sample.

Theoretical studies of how the shape and size of Si structures affect the band gap have been performed using a variety of approaches.<sup>33-46</sup> Generally speaking, the emphasis of these studies is on wirelike structures  $\gtrsim 20\text{ \AA}$  because these correspond to the typical shapes and smallest dimensions previously reported.<sup>13-16,21-27</sup> Band gaps calculated for wirelike sizes of, e.g.,  $15\text{ \AA}$ , fall in the range of 2.3–3.9 eV and grow substantially larger for smaller dimensions and for particlelike structures. Since these band gaps are much larger than any observed visible luminescence energy, the calculations generally serve to reinforce the reports of structural features with dimensions larger than  $15\text{ \AA}$ . Other developments growing out of comparisons with experimental results include an appreciation of how the confined electron-hole ( $e-h$ ) interaction lowers the effective transition energy<sup>33,46,96</sup> and how defect states in the gap might be involved in the transition.<sup>97</sup>

Assuming that defect states are not involved, there is obviously disagreement between our results and almost all previous theoretical work.<sup>34-38,41-46</sup> Not only do we maintain that particle rather than wirelike structures are the dominant shapes responsible for visible luminescence, but we find that their dimensions are even smaller than  $15\text{ \AA}$ . The calculated band gaps for such small particles range between 2.6 and 5 eV. Inclusion of the  $e-h$  interaction improves the situation, but not nearly enough. The three calculations<sup>33,39,40</sup> providing the closest agreement with our data are argued<sup>46</sup> to have underestimated the band gap because of oversimplification or error.

Recently, a different theoretical approach<sup>98</sup> has been applied to calculating electronic properties of Si nano-

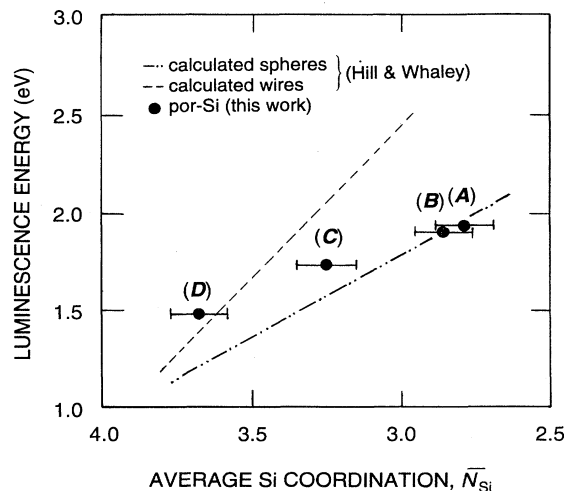


FIG. 17. Theoretical luminescence energy vs average Si coordination number for spherical particles and wires, from Ref. 62. Experimental values are from this work, Fig. 13.

structures.<sup>62,63</sup> In Fig. 17 we plot the so-calculated band gaps (including the  $e$ - $h$  interaction energy<sup>96</sup>) as a function of the  $\bar{N}_{\text{Si}}$  values corresponding to the differently shaped structures. This plot is similar to Fig. 13, and we include our por-Si results from that figure for comparison. The agreement between theory and experiment is very good, comparable to the excellent agreement found very recently between similar calculations<sup>63</sup> applied to spherical  $\text{Si}_x$  nanocrystals and our results from Fig. 5. These latest calculations imply that band-to-band transitions are indeed possible and that defect states are not necessary to explain the observed luminescence from por-Si. They also support our conclusions regarding the size, shape, and composition of the visible-light-emitting structures in these nanosized Si systems.

## V. CONCLUSIONS

It is ironic that of the many forms in which elemental Si is found—bulk crystalline, amorphous, polymeric, nanocrystalline, molecular, and porous—only the first has negligible quantum efficiency, even at low temperatures. The relatively high quantum efficiency of por-Si at room temperature has made it the focus of many different studies ranging from optoelectronic materials and device technology to fundamental properties of light-emitting Si nanostructures. These different studies share at least two common concerns: What is the species, and ultimately the mechanism, responsible for the room-temperature emission of visible light in nanosized Si systems? Why do they exhibit such high quantum efficiencies relative to that in bulk  $c$ -Si?

We have addressed the first of these issues by characterizing the geometric structure and composition of the optically active species in por-Si, using as a reference the

more well-defined case of surface-oxidized Si nanocrystals. X-ray-absorption spectroscopy and a variety of complementary and/or confirmatory methods were applied to both systems, yielding the following picture: The dominant species responsible for peak visible emission ( $< 700$  nm) are particles of locally crystalline Si whose average characteristic dimensions are smaller than 15 Å and whose surfaces are passivated with either H or O or both. Our results are consistent with the visible luminescence mechanism involving simple volume quantum confinement, as originally proposed.<sup>8,9</sup>

In addressing the second of these issues, we have recently argued that band-to-band transitions occur more efficiently in the nanostructures because there is a significant decrease in the radiationless transitions (Auger and defect recombination) that ordinarily quench bulk  $c$ -Si emission.<sup>78</sup> The coupling strength to the radiation field is actually not much stronger in either  $\text{Si}_x$  or por-Si. Both systems remain indirect-gap-like down to the smallest sizes studied.

## ACKNOWLEDGMENTS

We thank M. Stutzmann for discussions about photoinduced oxidation, and N. Hill for unpublished results. S.S. is grateful to the Alexander-von-Humboldt Foundation for financial support. The EXAFS experiments were performed at the National Synchrotron Light Source, Brookhaven National Laboratory, which is supported by the DOE, Division of Materials Sciences and Division of Chemical Sciences. The TEM measurements were performed at the National Center for Electron Microscopy, Lawrence Berkeley Laboratory, and were supported by the Director, Office of Basic Energy Sciences, DOE, under Contract No. DEAC03-76SF00098.

\*Present address: INFP, Forschungszentrum Karlsruhe, D-76021 Karlsruhe, Germany.

†Present address: Department of Applied Physics, Stanford University, Stanford, CA 94305.

‡Present address: Department of Materials Science, University of Illinois, Urbana-Champaign, IL 61801.

§Author to whom all correspondence should be addressed.

<sup>1</sup>J. I. Pankove, *Optical Processes in Semiconductors*, 2nd ed. (Dover, New York, 1974).

<sup>2</sup>H. Schangenotto, H. Maeder, and W. Gerlach, *Phys. Status Solidi A* **21**, 357 (1974).

<sup>3</sup>S. Iyer and Y.-H. Xie, *Science* **40**, 260 (1993).

<sup>4</sup>J. P. Noel, N. L. Rowell, D. C. Houghton, and D. D. Perovic, *Appl. Phys. Lett.* **57**, 1037 (1990).

<sup>5</sup>K. Terashima, M. Tajima, and T. Tatsumi, *Appl. Phys. Lett.* **57**, 1925 (1990).

<sup>6</sup>H. Ennen, J. Schneider, G. Pomerence, and A. A. Axmann, *Appl. Phys. Lett.* **43**, 943 (1983).

<sup>7</sup>H. Ennen, G. Pomerence, A. A. Axmann, K. Eisele, W. Hady, and J. Schneider, *Appl. Phys. Lett.* **46**, 381 (1985).

<sup>8</sup>L. T. Canham, *Appl. Phys. Lett.* **57**, 1046 (1990).

<sup>9</sup>V. Lehmann and U. Gösele, *Appl. Phys. Lett.* **58**, 856 (1991).

<sup>10</sup>R. Herino, G. Bomchil, K. Barla, C. Bertrand, and J. Ginoux, *J. Electrochem. Soc.* **134**, 1994 (1987).

<sup>11</sup>A. Bsiesy, J. C. Vial, F. Gaspard, R. Herino, M. Ligeon, F. Muller, R. Romestain, A. Wasiela, A. Halimaoui, and G. Bomchil, *Surf. Sci.* **254**, 195 (1991).

<sup>12</sup>J. C. Vial, A. A. Bsiesy, F. Gaspard, R. Herino, M. Ligeon, F. Muller, R. Romestain, and R. M. Macfarlane, *Phys. Rev. B* **45**, 14 171 (1992).

<sup>13</sup>M. I. J. Beale, N. G. Chew, M. J. Uren, A. G. Cullis, and J. D. Benjamin, *Appl. Phys. Lett.* **46**, 86 (1985).

<sup>14</sup>M. I. J. Beale, J. D. Benjamin, M. J. Uren, N. G. Chew, and A. G. Cullis, *J. Cryst. Growth* **73**, 622 (1985).

<sup>15</sup>G. Bomchil, A. Halimaoui, and R. Herino, *Microelectron. Eng.* **8**, 293 (1988).

<sup>16</sup>A. G. Cullis and L. T. Canham, *Nature* **353**, 335 (1991).

<sup>17</sup>For example, see *Light Emission from Silicon*, edited by S. S. Iyer, R. T. Collins, and L. T. Canham, MRS Symposia Proceedings No. 256 (Materials Research Society, Pittsburgh, 1992); *Microcrystalline Semiconductors: Materials Science & Devices*, edited by P. M. Fauchet, C. C. Tsai, L. T. Canham, I. Shimizu, and Y. Aoyagi, MRS Symposia Proceedings No. 283 (Materials Research Society, Pittsburgh, 1993); *Silicon-Based Optoelectronic Materials*, edited by M. A. Tischler, R. T. Collins, M. L. Thewalt, and G. Abstreiter, MRS Symposia Proceedings No. 298 (Materials Research Society, Pittsburgh, 1993); *Microcrystalline and Nanocrystalline*

- Semiconductors*, edited by R. W. Collins, C. C. Tsai, M. Hirose, F. Koch, and L. Brus, MRS Symposia Proceedings No. 358 (Materials Research Society, Pittsburgh, 1995).
- <sup>18</sup>L. E. Brus, *Appl. Phys. A* **53**, 465 (1991); *J. Phys. Chem.* **98**, 3575 (1994).
  - <sup>19</sup>H. Weller, *Angew. Chem. Int. Ed. Engl.* **105**, 41 (1993).
  - <sup>20</sup>N. Herron, J. C. Calabrese, W. E. Farneth, and Y. Wang, *Science* **259**, 1426 (1993).
  - <sup>21</sup>S.-F. Chuang, S. D. Collins, and R. L. Smith, *Appl. Phys. Lett.* **55**, 1540 (1989).
  - <sup>22</sup>R. L. Smith and S. D. Collins, *J. Appl. Phys.* **71**, R1 (1992).
  - <sup>23</sup>P. C. Searson, J. M. Macaulay, and S. M. Prokes, *J. Electrochem. Soc.* **139**, 3373 (1992).
  - <sup>24</sup>Y.-H. Xie, W. L. Wilson, F. M. Ross, J. A. Mucha, E. A. Fitzgerald, J. M. Macaulay, and T. D. Harris, *J. Appl. Phys.* **71**, 2403 (1992).
  - <sup>25</sup>Z. Sui, P. P. Leong, I. P. Herman, G. S. Higashi, and H. Tempkin, *Appl. Phys. Lett.* **60**, 2086 (1992).
  - <sup>26</sup>M. W. Cole, J. F. Harvey, R. A. Lux, D. W. Eckart, and R. Tsu, *Appl. Phys. Lett.* **60**, 2800 (1992).
  - <sup>27</sup>F. Kozlowski and W. Lang, *J. Appl. Phys.* **72**, 5401 (1992).
  - <sup>28</sup>K. H. Beckman, *Surf. Sci.* **3**, 314 (1965).
  - <sup>29</sup>M. A. Tischler, R. T. Collins, J. H. Stathis, and J. C. Tsang, *Appl. Phys. Lett.* **60**, 639 (1992).
  - <sup>30</sup>Z. Y. Xu, M. Gal, and M. Gross, *Appl. Phys. Lett.* **60**, 1375 (1992).
  - <sup>31</sup>H. Nishitani, H. H. Nakata, Y. Fujiwara, and T. Ohyama, *Jpn. J. Appl. Phys.* **31**, L1577 (1992).
  - <sup>32</sup>D. E. Aspnes and A. A. Studna, *Phys. Rev. B* **27**, 985 (1983). Depths have been crudely estimated by multiplying by 5 to account for the 80% porosity.
  - <sup>33</sup>M. V. Rama Krishna and R. A. Friesner, *J. Chem. Phys.* **96**, 873 (1992).
  - <sup>34</sup>A. J. Read, R. J. Needs, K. J. Nash, L. T. Canham, P. D. J. Calcott, and A. Qteish, *Phys. Rev. Lett.* **69**, 1232 (1992); **70**, 2050(E) (1993).
  - <sup>35</sup>F. Buda, J. Kohanoff, and M. Parrinello, *Phys. Rev. Lett.* **69**, 1272 (1992).
  - <sup>36</sup>T. Ohno, K. Shiraishi, and T. Ogawa, *Phys. Rev. Lett.* **69**, 2400 (1992).
  - <sup>37</sup>G. D. Sanders and Y. C. Chang, *Appl. Phys. Lett.* **60**, 2525 (1992); *Phys. Rev. B* **45**, 9202 (1992).
  - <sup>38</sup>J. P. Proot, C. Delerue, and G. Allan, *Appl. Phys. Lett.* **61**, 1948 (1992).
  - <sup>39</sup>T. Takagahara and K. Takeda, *Rev. B* **46**, 15 578 (1992).
  - <sup>40</sup>S. Y. Ren and J. D. Dow, *Phys. Rev. B* **45**, 6492 (1992).
  - <sup>41</sup>M. Hirao, T. Udo, and Y. Murayama, in *Microcrystalline Semiconductors: Materials Science & Devices* (Ref. 17), p. 425.
  - <sup>42</sup>B. Delley and D. F. Steigmeier, *Phys. Rev. B* **47**, 1397 (1993).
  - <sup>43</sup>F. Huaxiang, Y. Ling, and X. Xide, *J. Phys. Condens. Matter* **5**, 1221 (1993).
  - <sup>44</sup>C. Delerue, G. Allan, and M. Lannoo, *Phys. Rev. B* **48**, 11 024 (1993).
  - <sup>45</sup>C.-Y. Yeh, S. B. Zhang, and A. Zunger, *Appl. Phys. Lett.* **63**, 3455 (1993).
  - <sup>46</sup>L.-W. Wang and A. Zunger, *J. Phys. Chem.* **98**, 2158 (1994).
  - <sup>47</sup>S. Schuppler, S. L. Friedman, M. A. Marcus, D. L. Adler, Y.-H. Xie, F. M. Ross, T. D. Harris, W. L. Brown, Y. J. Chabal, L. E. Brus, and P. H. Citrin, *Phys. Rev. Lett.* **72**, 2648 (1994).
  - <sup>48</sup>A. Erbil, G. S. Cargill, R. Frahm, and R. F. Boehme, *Phys. Rev. B* **37**, 2450 (1988).
  - <sup>49</sup>S. L. Friedman, M. A. Marcus, D. L. Adler, Y.-H. Xie, T. D. Harris, and P. H. Citrin, *Appl. Phys. Lett.* **62**, 1934 (1993).
  - <sup>50</sup>P. A. Lee, P. H. Citrin, P. Eisenberger, and B. M. Kincaid, *Rev. Mod. Phys.* **53**, 769 (1981).
  - <sup>51</sup>C. Pickering, M. I. J. Beale, D. J. Robbins, P. J. Pearson, and R. Greef, *J. Phys. C* **17**, 6536 (1984).
  - <sup>52</sup>J. M. Perez, J. Villalobos, P. McNeil, J. Prasad, R. Cheek, J. P. Estera, P. D. Stevens, and R. Glosser, *Appl. Phys. Lett.* **61**, 563 (1992).
  - <sup>53</sup>E. Bustarret, M. Ligeon, and L. Ortéga, *Solid State Commun.* **83**, 461 (1992).
  - <sup>54</sup>M. S. Brandt, H. D. Fuchs, M. Stutzmann, J. Weber, and M. Cardona, *Solid State Commun.* **81**, 307 (1992).
  - <sup>55</sup>Y. Takeda, S. Hyodo, N. Sujuki, T. Motohiro, T. Hioki, and S. Noda, *J. Appl. Phys.* **73**, 1924 (1993).
  - <sup>56</sup>S. M. Prokes and O. J. Glembocki, *Phys. Rev. B* **49**, 2238 (1994).
  - <sup>57</sup>L. N. Dinh, L. L. Case, M. Balooch, L. J. Terminello, and F. Wooten, *Appl. Phys. Lett.* **65**, 1 (1994).
  - <sup>58</sup>W. E. Carlos and S. M. Prokes, *Appl. Phys. Lett.* **65**, 1245 (1994).
  - <sup>59</sup>Y. Kanemitsu, T. Ogawa, K. Shiraishi, and K. Takeda, *Phys. Rev. B* **48**, 4883 (1993).
  - <sup>60</sup>Y. Kanemitsu, *Phys. Rev. B* **48**, 12 357 (1993); **49**, 16 845 (1994).
  - <sup>61</sup>M. Koós, I. Pócsik, and É. Vázsonyi, *Appl. Phys. Lett.* **62**, 1797 (1993).
  - <sup>62</sup>N. A. Hill and K. B. Whaley, *Appl. Phys. Lett.* (to be published).
  - <sup>63</sup>N. A. Hill and K. B. Whaley, *Phys. Rev. Lett.* (to be published).
  - <sup>64</sup>K. A. Littau, P. F. Szajowski, A. J. Muller, A. R. Kortan, and L. E. Brus, *J. Phys. Chem.* **97**, 122 (1993); W. L. Wilson, P. F. Szajowski, and L. E. Brus, *Science* **262**, 1242 (1993).
  - <sup>65</sup>Y. H. Xie, M. S. Hybertsen, W. L. Wilson, S. A. Ipri, G. E. Carver, W. L. Brown, E. Dons, B. E. Weir, A. R. Kortan, G. P. Watson, and A. J. Liddle, *Phys. Rev. B* **49**, 5386 (1994).
  - <sup>66</sup>A. A. MacDowell, T. Hashizume, and P. H. Citrin, *Rev. Sci. Instrum.* **60**, 1901 (1989).
  - <sup>67</sup>L. G. Parratt, C. F. Hempstead, and E. L. Jossem, *Phys. Rev.* **105**, B1228 (1957).
  - <sup>68</sup>L. C. Feldman and J. W. Mayer, *Fundamentals of Surface and Thin Film Analysis* (Elsevier, New York, 1986).
  - <sup>69</sup>Y. J. Chabal, E. E. Chaban, and S. B. Christman, *J. Electron Spectrosc. Relat. Phenom.* **29**, 35 (1983); J. E. Reutt-Robey, D. J. Doren, Y. J. Chabal, and S. B. Christman, *J. Chem. Phys.* **93**, 9113 (1990).
  - <sup>70</sup>N. J. Harrick, *Internal Spectroscopy* (Wiley, New York, 1967), p. 30.
  - <sup>71</sup>C. Pickering, M. I. J. Beale, D. J. Robbins, P. J. Pearson, and R. Greef, *Thin Solid Films* **125**, 157 (1985).
  - <sup>72</sup>I. Sagnes, A. Halimaoui, G. Vincent, and P. A. Badoz, *Appl. Phys. Lett.* **62**, 1155 (1993).
  - <sup>73</sup>J. R. Chelikowsky, T. J. Wagener, J. H. Weaver, and A. Jin, *Phys. Rev. B* **40**, 9644 (1989).
  - <sup>74</sup>The incompletely developed band structure in even the largest ox-Si<sub>x</sub> nanocrystal, which is about 80 Å across, is apparently a consequence of crystal twinning in the internal Si<sub>x</sub> core.
  - <sup>75</sup>Like the nanocrystallites, the por-Si sample also consists of structures whose band structures are not fully developed due to their small size. Our results in Fig. 3 are completely unaffected by the choice of por-Si rather than c-Si because only difference spectra in the region > 1849 eV are being compared.
  - <sup>76</sup>Small artifactual structures near the bulk Si and SiO<sub>2</sub> peak absorptions at ~ 1840 and ~ 1847 eV are due to imperfect modeling by these pure constituents.

- <sup>77</sup>Densities and molecular weights for bulk *c*-Si, SiO<sub>2</sub>, and SiO were used, i.e., 2.33, 2.4, and 2.1 g per cm<sup>3</sup>, respectively.
- <sup>78</sup>L. E. Brus, P. F. Szajowski, W. L. Wilson, T. D. Harris, S. Schuppler, and P. H. Citrin, *J. Am. Chem. Soc.* **117**, 2915 (1995).
- <sup>79</sup>Etching *n*-type Si produces entirely different structures, e.g., straight, square-sided channels that are hundreds of Å to microns in length, cf. Refs. 21 and 22.
- <sup>80</sup>G. Bomchil, A. Halimaoui, I. Sagnes, P. A. Badoz, I. Berbezier, P. Perret, B. Lambert, G. Vincent, L. Garchery, and J. L. Regolini, *Appl. Surf. Sci.* **65/66**, 394 (1993).
- <sup>81</sup>O. Teschke, M. C. Goncalves, and F. Galembeck, *Appl. Phys. Lett.* **63**, 1348 (1993).
- <sup>82</sup>F. M. Ross, J. M. Gibson, and R. D. Twesten, *Surf. Sci.* **310**, 243 (1994).
- <sup>83</sup>J. A. Schaefer, D. Frankel, F. Stucki, W. Göpel, and G. J. Lapeyre, *Surf. Sci.* **139**, L209 (1984).
- <sup>84</sup>Y. J. Chabal, G. S. Higashi, K. Raghavachari, and V. A. Burrows, *J. Vac. Sci. Technol. A* **7**, 2104 (1984).
- <sup>85</sup>Over the course of 10-min radiation exposure, we did not observe a degradation of luminescent intensity (Refs. 29 and 86) or a photoinduced luminescence enhancement (Ref. 87). These effects, which depend on radiation power and sample preparation, required extended exposure times.
- <sup>86</sup>R. T. Collins, M. A. Tischler, and J. H. Stathis, *Appl. Phys. Lett.* **61**, 1649 (1992).
- <sup>87</sup>S. Shih, K. H. Jung, J. Yan, D. L. Kwong, M. Kovar, J. M. White, T. George, and S. Kim, *Appl. Phys. Lett.* **63**, 3306 (1993).
- <sup>88</sup>R. A. Street, *Hydrogenated Amorphous Silicon* (Cambridge University Press, Cambridge, 1991).
- <sup>89</sup>The effective sampling depth is not linear with energy, as it depends on the energy loss of the He<sup>+</sup> ions traveling to the point of recoil and the recoiling H atoms traveling from that point to the surface.
- <sup>90</sup>A. V. Rao, F. Ozanam, and J.-N. Chazalviel, *J. Electrochem. Soc.* **138**, 153 (1991).
- <sup>91</sup>Because the grazing-incidence data have been approximately scaled to the transmission data, absolute intensity comparisons between the two cannot be made.
- <sup>92</sup>Some shapes, such as tetrahedra, could fall outside the lines, but these are considered unlikely structures.
- <sup>93</sup>P. D. J. Calcott, K. J. Nash, L. T. Canham, M. J. Kane, and D. Brumhead, *J. Phys. Condens. Matter* **5**, L99 (1993).
- <sup>94</sup>In fact, the *S/V* ratio of a sphere with diameter *L*, namely  $6/L$ , is identical to that of a cube with side *L*. The reason for the small differences in Fig. 14 between these two shapes is due to the finite nature of the Si-Si bonds.
- <sup>95</sup>For a Si cube of side *L*,  $N(\text{Si})_{\text{cube}} = 8L^3/a_0^3$ ; for a sphere of diameter *L*,  $N(\text{Si})_{\text{sphere}} = (\pi/6)\{N(\text{Si})_{\text{cube}}\}$ .
- <sup>96</sup>L. E. Brus, *J. Chem. Phys.* **80**, 4403 (1984).
- <sup>97</sup>F. Koch, V. Petrova-Koch, T. Muschik, A. Nikolov, and V. Gavrilenko, in *Microcrystalline Semiconductors: Materials Science & Devices* (Ref. 17), p. 197.
- <sup>98</sup>N. A. Hill and K. B. Whaley, *J. Chem. Phys.* **99**, 3707 (1993); **100**, 2831 (1994).

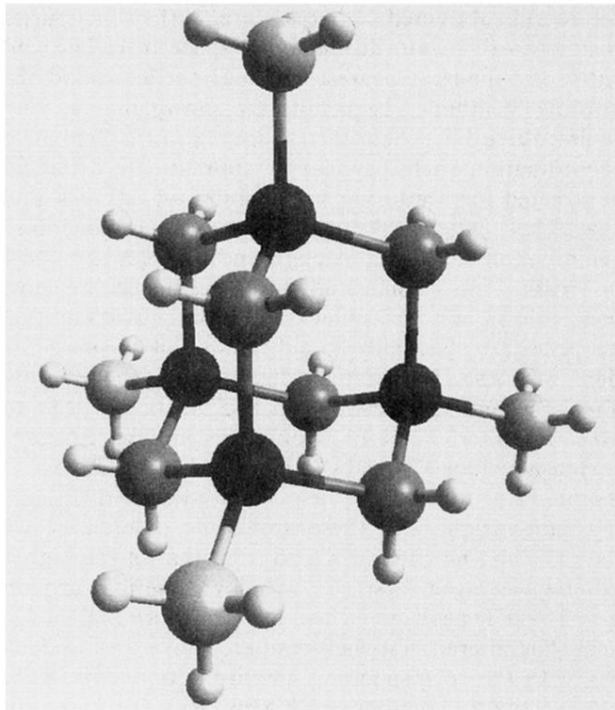


FIG. 10. Hypothetical  $\text{Si}_{14}\text{H}_{32}$  cluster/molecule. Darkest spheres are (bulk) Si atoms coordinated to the other four Si atoms, and lighter spheres are (surface) Si atoms coordinated to either two or three H atoms, which are represented by the smaller, lightest spheres. In this  $\approx 8\text{-\AA}$  cluster, the average Si coordination  $\bar{N}_{\text{Si}}$  is 2.29, and the H/Si ratio is 1.71.

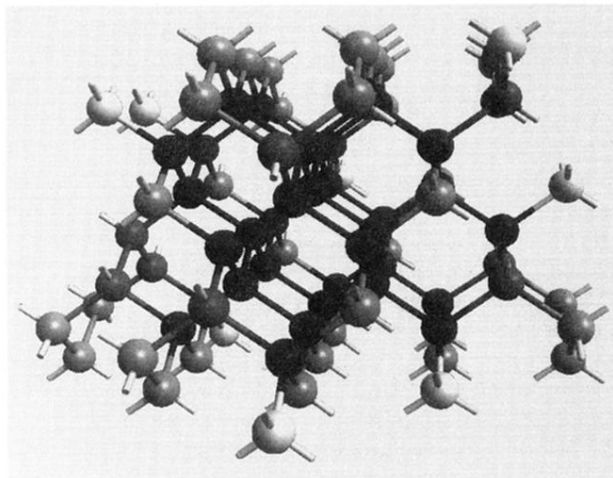
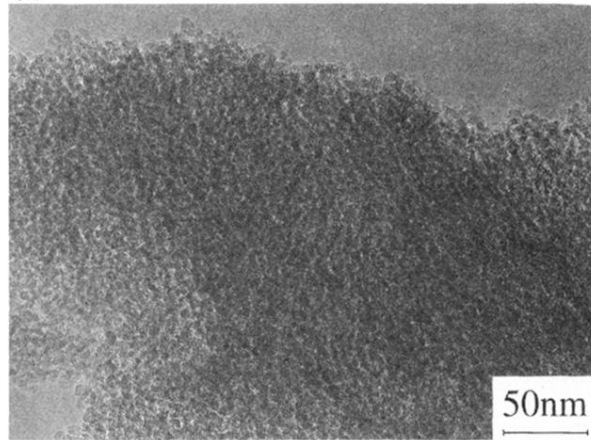


FIG. 16. A typical visible-light-emitting por-Si structure. Its characteristic size is about 13 Å and its shape is approximately rectangular with predominantly (100) surfaces. All dangling bonds of surface Si atoms, shown unpassivated, are presumed passivated mainly with H atoms in freshly prepared material (some bonds must obviously be connected to other Si atoms of adjacent por-Si structures in an actual sample). Of the 86 Si atoms, only 35 (dark) are bulklike, with a Si coordination of 4. The average Si coordination in this structure is 2.79, very similar to that measured in the por-Si (A) sample.



(a)



(b)

FIG. 6. (a) Large-scale structure of por-Si (*B*), obtained with bright-field (110) image of an ion-milled cross-sectional specimen. The porous material, seen within two well-defined cylindrical regions, shows a mottled contrast. Apart from the overall film thickness, por-Si (*A*) and por-Si (*C*) samples appear similar at this magnification. (b) Small-scale structure of por-Si (*C*). The porous region is composed of granular features with 30–60-Å characteristic sizes. There is some variability in the feature size at different parts of the layer. por-Si (*A*) and por-Si (*B*) samples appear identical in the TEM micrographs.